JGR Oceans

RESEARCH ARTICLE

10.1029/2025JC023311

Field Observations of Intermittent Cross-Shore Bed Load Transport on a Low-Energy Beach

Marlies van der Lugt[1,2], Noémie Fritsch[3], Matthieu de Schipper[1], Ad Reniers[1], Meagan Wengrove[4], and France Floc'h[3]

[1]Department of Hydraulic Engineering, Faculty of Civil Engineering and Geosciences, TU Delft, Delft, The Netherlands, [2]Department of Applied Morphodynamics, Deltares, Delft, The Netherlands, [3]Univ Brest, CNRS, Geo-Ocean UMR6538, Plouzané, France, [4]School of Civil and Construction, Oregon State University, Corvallis, OR, USA

Key Points:

- Sea- and shoreward cross-shore bed load sediment transport measured by tracking vortex-ripple migration on a low-energy beach
- Field observations of mean flow direction reversal between free-stream and the wave bottom boundary layer on top of vortex ripples
- Including phase-coupled long wave variance in a bed load model proved essential to capture moments of offshore ripple migration

Correspondence to:

M. van der Lugt,
m.a.vanderlugt@tudelft.nl

Citation:

van der Lugt, M., Fritsch, N., de Schipper, M., Reniers, A., Wengrove, M., & Floc'h, F. (2026). Field observations of intermittent cross-shore bed load transport on a low-energy beach. *Journal of Geophysical Research: Oceans*, *131*, e2025JC023311. https://doi.org/10.1029/2025JC023311

Received 15 AUG 2025
Accepted 28 APR 2026

Author Contributions:

Conceptualization: Marlies van der Lugt, Matthieu de Schipper
Data curation: Marlies van der Lugt
Funding acquisition: Matthieu de Schipper, France Floc'h
Investigation: Marlies van der Lugt, Noémie Fritsch
Methodology: Marlies van der Lugt, Noémie Fritsch, Matthieu de Schipper, Meagan Wengrove
Resources: France Floc'h
Supervision: Matthieu de Schipper, Ad Reniers
Writing – original draft: Marlies van der Lugt
Writing – review & editing: Matthieu de Schipper, Ad Reniers, Meagan Wengrove, France Floc'h

Abstract Low-energy sandy beaches typically have a rippled bed, and the presence of bed forms can strongly affect net sediment transport rates under combined forcing of waves and currents. In case low-energetic forcing is combined with coarse sediment, bed load transport is an important mechanism to understand transport processes on such beaches. This study presents observations of ripple geometry and migration from a low-energy beach composed of coarse sediment ($D = 630$ μm) in the bed load transport regime. The concurrent hydrodynamics were monitored with free-stream point measurements of velocity and pressure, and with velocity profiles from 15 cm above the bed into the wave boundary layer. The bed was rippled with relic and orbital vortex ripples. Cross-shore bed load transport associated with ripple migration was highly intermittent and alternating in direction. A bed load sediment transport model forced with the measured free-stream velocity signal led to a consistent overprediction of offshore directed transport. Using the measured velocities excluding the mean cross-shore velocity, the model captured the correct direction of all but one observed instance of migration in our data set. Velocity profiles confirmed that mean free-stream velocity was not representative of the magnitude and at times the direction of the mean flow in the wave bottom boundary layer over a rippled bed. Phase coupling between sea-swell and infragravity frequencies in orbital velocity forcing proved essential to capture the cross-shore bed load direction.

Plain Language Summary The nearshore sea bed can be flat or rippled and is constantly in motion due to wind and waves. Ripples on the bed exist when the wave and currents are relatively calm, and become more pronounced if the sand is coarse-grained. This study presents observations of ripple height, length, orientation and migration from a beach that is sheltered from open coast waves and consists of very coarse sand. We discuss the ripple migration patterns in the context of the prevailing hydrodynamic forcing. In the alongshore direction the ripple migration correlated with the alongshore mean flow, but this was not the case in the cross-shore direction. We made observations of the velocity profile very near the bed and showed that the mean flow direction in the boundary layer near the bed was sometimes opposite to the direction in the rest of the water column. A bed load transport model (thus entailing rolling, sliding or hopping of sand grains, but not their transport in suspension) that did not include the cross-shore mean velocity showed good skill in describing the direction of observed ripple migration. The asymmetry of the wave motions in the water column proved essential to capture the cross-shore bed load direction.

1. Introduction

The presence of ripples on the bed strongly affects net sediment transport rates under combined forcing of waves and currents (Andersen, 1999; Thorne et al., 2003; Van Der Werf et al., 2007). Not only do ripples increase bed shear stress by adding form drag to skin friction (Soulsby, 1997), their interaction with the flow can completely alter the direction of net transport (Ribberink et al., 2008). When ripples are sufficiently steep and the forcing is energetic enough, sediment-laden vortices are ejected from between the ripples into the water column (Frank-Gilchrist et al., 2024; Wang & Yuan, 2020), enhancing current-related suspended transport rates, while the presence of ripples under low energy but asymmetric wave forcing enhances wave-driven bed load transport rates (Van Der Werf et al., 2006).

At fetch limited, low-energy beaches, sediment transport is highly intermittent, neither wave- nor current dominated (Nordstrom & Jackson, 2012), and consequently the bed is generally rippled (Nielsen, 1981). Sandy beaches in low-energy environments have been found to have widely varying cross-shore beach profiles, which

may contain beach steps, berms and sharp transitions in profile steepness (e.g., Costas et al., 2005; Hegge et al., 1996; Makaske & Augustinus, 1998; Travers, 2007). Developing an over-arching understanding of the classification system based on sediment composition and offshore forcing conditions alone has proven difficult (Vila-Concejo et al., 2020). As beach profile characteristics ultimately result from the underlying transport processes, this suggests that improving understanding of the local transport processes and balance therein is essential to understand the sediment balance (Vila-Concejo et al., 2024).

There are a fair amount of observations of suspended transport in the field (e.g., Brinkkemper et al., 2018; De Bakker et al., 2016; Osborne & Greenwood, 1992; Ruessink et al., 1998), but direct measurements of bed load are scarce in the field, partly due to the difficulty of measuring concentration and velocity very close to a mobile bed. As a result, bed load transport is mostly studied in laboratory studies (e.g., Fritsch et al., 2024; Mieras et al., 2019; Ribberink et al., 2008). The translation of laboratory results to the field is not trivial, as in the field, wave forcing is irregular, directional and progressive. Although bed load is difficult to measure through direct methods, we can exploit the fact that ripple migration is one mechanism of bed load transport (Guerrero et al., 2021; Kalra et al., 2022; Van Rijn, 2007), and we can use it to estimate the direction and volume of bed load transport (Hoekstra et al., 2004; Traykovski et al., 1999). Understanding the drivers of ripple migration therefore aids the understanding of net bed load transport.

The aim of this study is therefore to explore the relation between hydrodynamic forcing, ripple geometry and migration in the shoaling zone of a fetch-limited, low-energy field site. We use ripple migration as proxy for bed load transport to evaluate the processes driving bed load transport in low energy-conditions.

1.1. Ripple Regimes

Ripples are generally classified based on how their geometry responds to changes in forcing. Orbital ripples have ripple wave length and height scale with near-bed orbital excursion, where anorbital ripple wavelength is only a function of the sediment composition (Clifton & Dingler, 1984). In the transition regime between orbital and anorbital ripples the ripple wavelength (λ) scales with both orbital excursion (d_0) and grain size (D) and this regime is referred to as suborbital ripples (Clifton & Dingler, 1984). Ripple steepness (η/λ, with η being ripple height) indicates whether vortices can be shed from the ripple troughs. A threshold for vortex ripples is estimated at steepness larger than $\eta/\lambda > 0.12$. Ripples with lower steepness are referred to as rolling grain ripples, which can be a result of either very mild forcing conditions just above the threshold of motion (pre-vortex ripples), or energetic conditions just before the onset to sheet flow (post-vortex ripples; Miller & Komar, 1980). Steepness of orbital vortex ripples is found to be fairly constant, typically around 0.15 (Nelson et al., 2013), but always in the range 0.12–0.22 (Bagnold, 1946).

1.2. Field Observed Ripple Migration

Ripple migration has been observed in the field and discussed in several studies with widely varying ripple and forcing regimes. Most of the time, ripples in the nearshore are observed to be onshore migrating (Hanes et al., 2001; Hoekstra et al., 2004; Masselink et al., 2007; Traykovski et al., 1999; Wengrove et al., 2018). Orbital velocity skewness is generally pointed to as the driving mechanism (Crawford & Hay, 2001; Kalra et al., 2022; Miles et al., 2014; Ngusaru & Hay, 2004), confirmed by observed absence of migration in the lower shoreface where velocity skewness was observed negligible (Guerrero et al., 2021). Some studies observed alternating patterns of onshore and offshore migration (Becker et al., 2007), but there is no consensus on the cause for offshore directed migration as studies either point to mean flow due to return currents (Doucette, 2002; Miles et al., 2014) or associate it with negative wave skewness (Crawford & Hay, 2001). Rates of migration varied greatly between studies, with a possible explanation being the large variety in wave driven oscillatory flow magnitudes, partly caused by differences in the water depth where observations are made (Austin et al., 2007).

2. Methods

2.1. Field Site and Instrumentation

The field campaign was set-up on the man-made beach "Prins Hendrik Zanddijk" (PHZD) located on the back-barrier side of the Wadden Island Texel along the Marsdiep estuary in the Netherlands. This site is sheltered from North Sea swell under most wind directions (Figure 1a). At this site, a sandy beach and dune have been

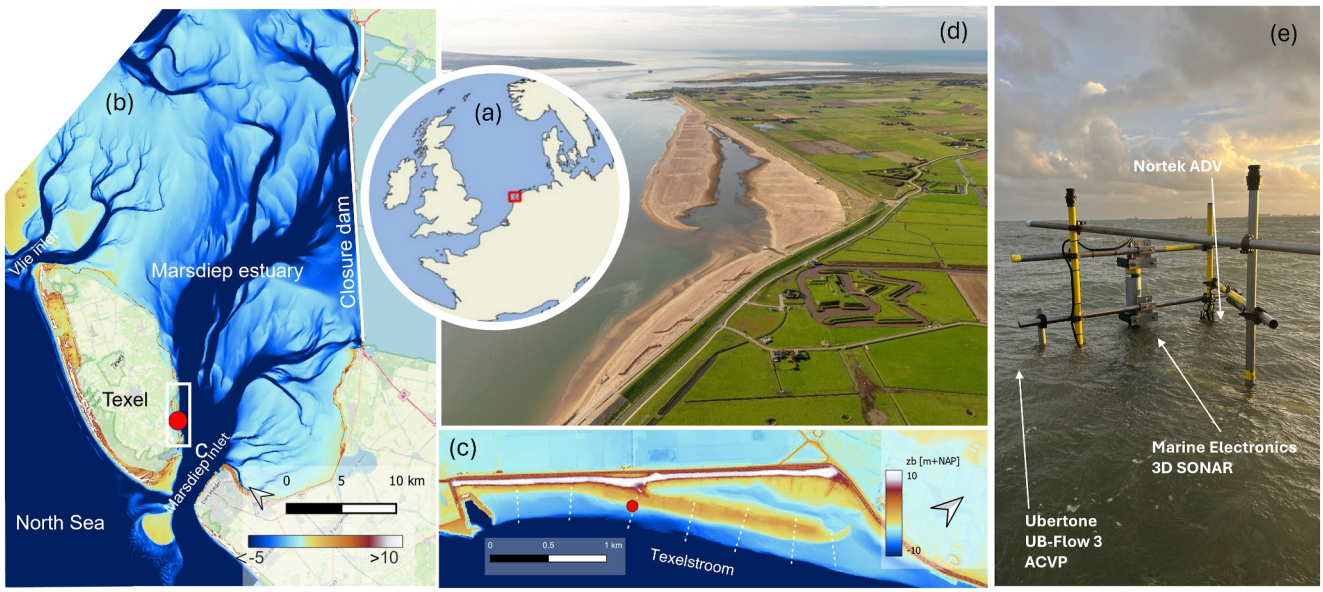

Figure 1. Field site and instrument setup. (a) Field site location in Europe indicated with red square, (b) estuarine bathymetry with the red dot outlining the position of the man-made beach, (c) detailed bathymetry of the man-made beach Prins Hendrik Zanddijk with the red dot indicating the position of the measurement frame (d) aerial photograph of the field site taken from North, (e) photograph of the instrument looking seaward with the mounting position of the three instruments.

constructed in 2019 on top of a naturally existing subtidal shoal with the purpose of acting as a wave dissipator under extreme conditions to protect the hinterland from flooding (Perk et al., 2019). Sediment at the site is a poorly sorted mixture with, at the location of the frame, a sediment composition with on average $D_{10} = 280$ µm, $D_{50} = 630$ µm and $D_{90} = 1090$ µm (Van Der Lugt, Bosma, et al., 2024). Further analysis herein uses $D = 630$ µm.

Storm Ciarán passed Texel island as a Beaufort scale 9 storm with wind speeds up to 115 km/hr from southerly directions on 2 October 2023. RTK-DGPS transect measurements one day before and one day after passing (3 October 2023) showed a loss of ∼1 m^3/m of sediment from the upper beach profile and an accumulation of ∼3 m^3/m below storm water level (NAP+1.46 m) in this section of the beach. In the week following the storm, a berm formed around the mean water line (Figure 2).

A day before the passing of storm Ciaràn, an instrument frame was placed at the beach step below the low water line of the sandy beach (Figure 2). At the location of the frame, the bed slope pre-storm was 1:30, but after the storm it steepened to 1:15 locally. Three instruments were mounted: a Marine Electronics 3D Sand Ripple Profile Scanner (SRPS), a Nortek Acoustic Doppler Velocimeter (ADV) and a newly developed downward-looking bistatic Ubertone UB-Flow 3D Acoustic Concentration and Velocity Profiler (ACVP). Originally developed for laboratory studies of near-bed and oscillatory unidirectional flows, this new version features a central emitter and four receivers (each at a distance 0.1 m from the emitter) operating at 1 MHz. The angle formed between the emitter/receiver axis and the vertical is 120°. Field deployments of bistatic acoustic velocity profiling instruments in the bottom boundary layer are sparse but emerging (Fritsch et al., 2026; Mignot et al., 2011) and exploit the ACVP principles that have been demonstrated successfully in the lab (Hurther & Thorne, 2011).

The ripple scanner's sonar head was mounted 75 cm above the bed, and programmed to scan every 15 min a cone of acoustic backscatter within a 90° arc, leading to a footprint of twice the distance of the head to the bed, with an arc-resolution of 0.9°, a rotational step of 1.8 ° and a radial resolution of 0.25 cm. The ADV's control volume was initially positioned at 30 cm above the bed. The elevation above the bed varied through ripple migration below the sensor and was reduced by sediment deposition in aftermath of the storm to 20 cm. The ADV was recording continuously at 16 Hz.

The ACVP was installed at 30 cm above the initial bed. In the present experiment, the acoustic and geometrical settings were set to measure velocities up to 2.0 m/s over a vertical profile of 20 cm with a vertical bin resolution of 2 mm and a sampling frequency of 51 Hz. The vertical profile was initially centered around the bed position:

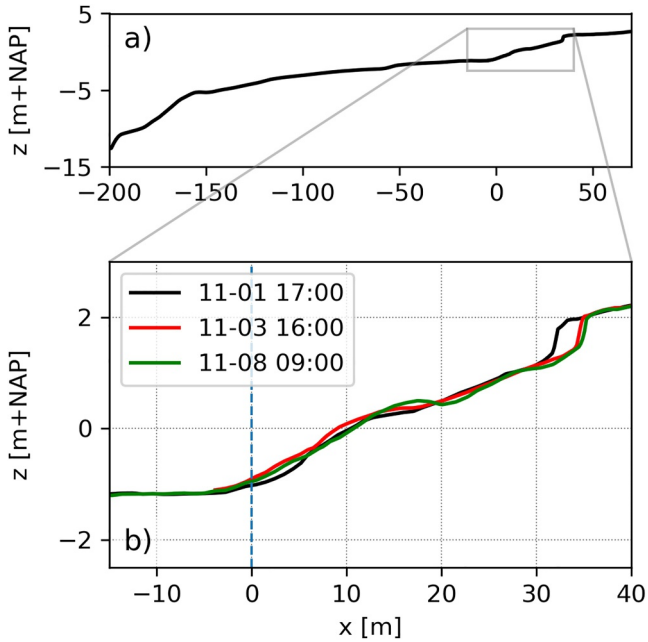

Figure 2. Cross-shore bed profile at transect with the measurement frame (a) with zoom of the profile around the water line (b) with the pre-storm elevation (black), post-storm profile (red) and profile 1 week after the storm (green). Blue vertical line indicates the location of the measurement frame.

10 cm above the bed and 10 cm into the bed, to ensure the boundary layer was also captured in case of some bed level change.

2.2. ADV Hydrodynamics

Following the time resolution of the SRPS scan interval, the continuous pressure and velocity measurements of the ADV were cut into 15 min regular blocks over which flow, wave and water level statistics were computed. At this site with short-period waves ($T < 6$ s), 15 min is sufficiently long for mean spectral wave statistics, including the infragravity component. Pressure was corrected for air pressure fluctuations, and instances where the instrument fell dry were removed from the data set. The pressure and velocity timeseries were quality checked and converted to sea-surface elevation using linear theory over the frequency range $[0.5f_p, 2f_p]$ Hz following the methodology as outlined in Van Der Lugt, De Schipper, et al. (2024). Mean water level (z_s) was computed as the block-mean sea-surface elevation. Significant wave height was then computed as $H_{m0} = 4\sqrt{m_0}$ and mean wave period $T_{m-1,0} = \frac{m_{-1}}{m_0}$ with m_n the spectral moment of order n of the sea-surface variance density spectrum. These wave spectra were calculated from the 900 s long blocks using 52 Hamming windows with 50% overlap, resulting in a frequency resolution of 0.03125 Hz. Combining the sea-surface elevation with the horizontal velocities, the mean wave direction ϑ_w was reconstructed using the method of maximum entropy (Lygre & Krogstadt, 1986). Horizontal velocities were then transformed in cross-shore and alongshore components $\mathbf{u} = (u_{cross}, u_{along})$. Block averaged mean flow direction is given by $\vartheta_c = \tan^{-1}(u_{along}/u_{cross})$.

Root-mean-square orbital velocity is computed as:

$$u_{\text{rms}} = \sqrt{\langle (u_d - \overline{u_d})^2 \rangle} \tag{1}$$

with u_d the sea-swell orbital velocity projected in the mean wave direction ϑ_w and $\langle . \rangle$ indicating the average over the block. With these quantities, the orbital excursion d_0 is estimated as:

$$d_0 = \frac{T_{m-1,0} u_{\text{rms}}}{\sqrt{2}\pi} \tag{2}$$

Orbital velocity skewness and asymmetry were computed as:

$$S_u = \langle u_d^3 \rangle / u_{\text{rms}}^3 \tag{3}$$

$$A_u = \langle \mathcal{H}(u_d)^3 \rangle / u_{\text{rms}}^3 \tag{4}$$

With $\mathcal{H}$ the Hilbert transform (Cizek, 1970). Positive values of S_u indicate larger onshore velocities under the wave crest and smaller offshore velocities under the wave through and negative values of A_u indicate larger acceleration from wave trough to crest than from crest to through.

Although the typical frequency range to investigate sea-swell orbital velocity is [0.05, 1] Hz, this range encompasses too many sub-gravity velocities for the wave periods encountered at this low-energy site and cuts off any super harmonics above 1 Hz, which could be bound to typically high peak frequencies observed. Therefore instead, we let the frequency band associated with sea swell scale with the block's peak frequency f_p: $[0.5f_p, f_{nyq}]$ Hz (f_p roughly varying between 0.25 and 0.5 Hz in these observations), in line with the approach in Van Der Lugt, De Schipper, et al. (2024).

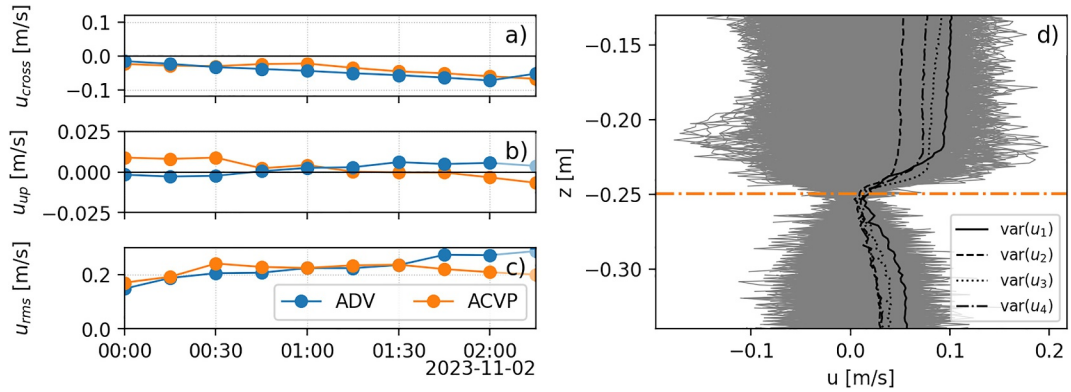

Figure 3. (a–c) Cross-validation of ACVP and ADV velocities in the free-stream at 15 min intervals. (a) Cross-shore flow velocity (positive velocities are onshore), (b) upward flow velocity, (c) root-mean-square orbital velocity. (d) Identification of position of the bottom: 1000 instantaneous recordings of velocity profiles from beam 1. Black lines (solid, dashed, dotted and dashed-dotted) are the gate-averaged velocity variance for beams 1–4. Orange dashed line indicates the identified bed level.

2.3. ACVP Hydrodynamics

The deployed ACVP requires a sufficient concentration of seedy material (sandy sediment) in the water column for a good signal-to-noise ration. This resulted in a single 2-hr event during the passage of a storm at low tide on 2023-11-02. During recovery of the instrument after this storm-deployment, it was noted that the instrument's mounting clamp was rotated over its alongshore-oriented mounting pole, possibly due to impact of a large wave on the bolts. As a result, the reconstructed velocity vector had to be corrected for imperfect alignment with the vertical. The required rotation angle (30°) to correct for this was found by rotating coordinate system in steps of 0.5° over the alongshore axis, minimizing the velocity variance in the direction of gravitational acceleration. All ACVP recordings with signal-to-noise ratio's below 3 were removed from the data set.

Free-stream mean velocity statistics as recorded by the ACVP were cross-validated to the ADV recordings. The ADV did not measure continuously throughout the storm: after 11-02 02:20 it was intermittently dry because of passing of wave troughs. Therefore, the cross-validation is done from the start of valid ACVP recordings (11-02 00:00) to 11-02 02:20. The instruments were separated by approximately 1.5 m in the alongshore direction but were installed at the same initial bed level contour. The top gates of the velocity profile of the ACVP are assumed to be free-stream recordings, at 15 cm above the bed; however, the free-stream observations of the ADV were 30 cm above the bed. ACVP measurements were aggregated to a vertical resolution of 1 cm. Both ADV and ACVP recordings were aggregated to a temporal resolution of 15 min. The timeseries of the second gate from the transducer of the ACVP was then compared to the ADV (Figures 3a–3c). The net offshore directed cross-shore flow component was comparable up to ±10% between instruments and were up to 0.08 m/s in magnitude within this time interval. Upward velocities are an order of magnitude smaller and no greater than 0.01 m/s for both instruments. Root-mean-square orbital velocities averaged at 0.2 m/s and compared well between instruments with differences up to 15%.

In this study, the ACVP measurements are used to study the near-bed mean flow velocity profile above a ripple that migrated onshore below the instrument. The ACVP measures all the way into the wave bottom boundary layer and into the bed, but only the velocity estimates above the bed are meaningful. The instantaneous position of the bed was identified as the vertical gate that minimized the raw velocity variance in the beam-directions, inspired by the methodology outlined in Puleo et al. (2012). For each of the 4 beams (one for each transducer), the velocity variance over a 1 s rolling window in time was computed, and the vertical level associated with the minimum in velocity variance saved. This timeseries of instantaneous bed level (still at 51 Hz) was then coarsened to 30 s (duration of roughly 10 waves passing) by identifying the vertical level associated with the 95th percentile of bed level height within the 30 s. The estimated bed positions from each of the four beams were then averaged to the final estimate of the bed position (Figure 3d).

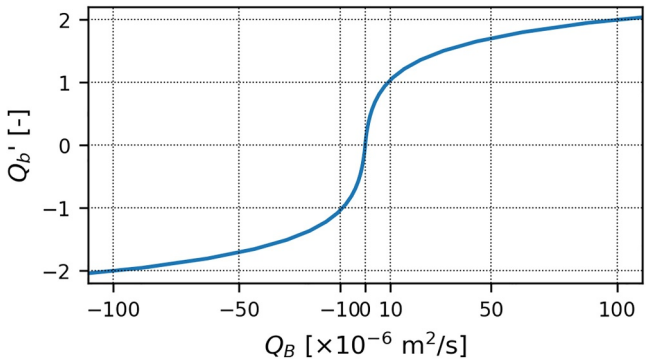

Figure 4. Visualization of the log-modulus transform (Equation 11).

2.4. Ripple Geometry Detection

Ripple geometry was extracted from the SRPS backscatter data following two approaches. The first methodology reconstructed 3D footprints of the bed and analyzed the power spectra of the footprints to extract estimates of ripple height η_{3D}, ripple length λ_{3D} and ripple orientation ϕ_{3D}, inspired by the procedure outlined in Wengrove et al. (2017). During calm wave conditions, some of the reconstructed footprints showed bed level anomalies in the wake of a frame pole from the tidal alongshore currents (e.g., Figure A1d, blue patch next to pole). In these conditions (about ∼25% of the time), the peak ripple length from the wavenumber power spectra could be compromised by these wake effects, whilst through manual visual observation of the footprints, a structured ripple field could still be discerned. To obtain good quality ripple statistics at these moments where a feature was present next to the instrument pole, a second 2D approach was followed in which swaths were analyzed separately, resulting in estimates η_{2D}, λ_{2D} and ϕ_{2D}. 2D and 3D estimates are both discussed in the manuscript. Ripple migration rates $\mathbf{v}_{mig} = (v_{mig,cross}, v_{mig,along})$ were estimated using 2D cross-correlation of the 3D footprints following Wengrove et al. (2017), as well as 1D cross-correlations on the swaths individually with $v_{mig,cross} = \cos(\phi_{2D})v_{mig,2D}$. Further processing details are discussed in Appendix A.

2.5. Ripple Volume Transport

Under the assumption that ripples transport their entire volume of sand with them, the volume transport associated with their migration can be computed as (e.g., Kalra et al., 2022; Traykovski et al., 1999; Wengrove et al., 2017):

$$\mathbf{q}_{ripple} = (1-\epsilon)\mathbf{v}_{mig}A\eta \tag{5}$$

with $\mathbf{q}_{ripple} = (q_{cross}, q_{along})$ the sediment transport rate in units of m^2/s, $\epsilon = 0.3$ the porosity, and A a ripple form factor. It is not always the case that the ripple migration pattern is related to the sediment transport direction, but this is a fair assumption to make in case shear stresses are low and transport occurs in the bed load regime, which are the conditions in this data set (Section 4.1). A is theoretically bound between 0 (periodic Dirac functions) and 1 (periodic block functions), and for ripples that maintain constant shape and are perfectly sinusoidal, $A = 0.5$. As forcing conditions are time-varying in the field, it is not expected that the ripples maintain their exact shape throughout the entire campaign, evidenced by the non-perfect scan-to-scan cross-correlation discussed in Appendix A. We treat the results from Equation 5 therefore as a first-order estimate of the direction and order of magnitude of the observed bed load transport.

2.6. Bed Load Sediment Transport

To investigate to what extent the bed load transport associated with the ripple migration can be understood from free-stream velocity observations, the contribution of bed load transport driven by velocity, horizontal pressure gradients as well as gravity driven transported is explored and compared to observations. Bed load sediment transport at this site is expected to be highly intermittent given the low-energy regime of the forcing and therefore models are selected that explicitly incorporates the threshold of motion. Ribberink (1998) proposed a bed load transport model assuming that bed load is the instantaneous result of prevailing waves and currents exceeding the threshold of motion:

$$\mathbf{Q_B}(t) = \sqrt{(\rho_s - \rho)gD_{50}^3}\,\mathbf{\Psi_B}(t) \tag{6}$$

With g gravitational acceleration, ρ_s sediment density, ρ water density and $\mathbf{\Psi_B}(t) = (\Psi_{cross}, \Psi_{along})(t)$ the dimensionless bed load transport rate computed as:

$$\Psi_{\mathbf{B}}(t) = \begin{cases} m(|\theta(t)| - \theta_{crit})^n \dfrac{\boldsymbol{\theta}(t)}{|\theta|(t)} & \text{for } |\theta|(t) > \theta_{crit} \\ 0 & \text{for } |\theta|(t) \leq \theta_{crit} \end{cases} \tag{7}$$

with θ_{crit} the critical Shields parameter (here computed with the expression of Soulsby (1997)) and $\boldsymbol{\theta}(t) = (\theta_{cross}, \theta_{along})(t)$ the instantaneous Shields parameter $\left(|\theta|(t) = \sqrt{\theta^2_{cross}(t) + \theta^2_{along}(t)}\right)$ associated with skin friction (form drag does not play a role in this bed load predictor):

$$\boldsymbol{\theta}(t) = \frac{1}{2}\rho \frac{f_w(t)|\mathbf{u}(t)|\mathbf{u}(t)}{gD_{50}(\rho_s - \rho)} \tag{8}$$

Here, the wave friction factor is $f_w(t) = \exp\left[5.213\left(\frac{2.5D_{50}}{d_0(t)}\right)^{0.194} - 5.977\right]$, as according to Swart (1974), with $d_0(t)$ the 15-min average orbital excursion and $\mathbf{u}(t) = (u_{cross}, u_{along})(t)$ the instantaneous (16 Hz) velocity signal. The calibration coefficients m and n were derived by regression on a combination of laboratory data sets and set at $m = 11$, $n = 1.65$ in Ribberink (1998). $n = 1.5$ (as proposed by Meyer-Peter and Mueller (1948), Fernandez Luque and Van Beek (1976), Nnadi and Wilson (1992)) directly relates the predicted sediment transport to third-order moments of the instantaneous velocity signal, but through the optimized fit from the Ribberink model this direct physical interpretation in the coefficients is lost.

The Ribberink model described bed load transport on a horizontal bed, while our measurements were taken at the beach step between a near-horizontal platform and a rather steep beach face. Throughout the measurement week, the local bed slope steepened from roughly 1:30 to 1:15. The bed slope is expected to affect the threshold of motion (Dey, 2003), but this effect is deemed negligible compared to the expected variability in θ_{crit} due to time-dependency of the instantaneous slope of the rippled bed and time-varying sediment properties which are unknown in these field observations. Shore parallel tidal currents were however continuously present and are expected to contribute to the cross-shore sediment balance through the gravity-driven transverse bed slope effect. This bed load contribution was explored using the model proposed by Talmon et al. (1995):

$$Q_{BG,n}(t) = -G\frac{\partial z_b}{\partial n}|Q_{B,s}|(t) \tag{9}$$

With $Q_{BG,n}(t)$ the additional gravity-driven down-slope bed load transport rate in the slope-normal direction as a result of slope-parallel bed load transport $Q_{B,s}(t)$, $\frac{\partial z_b}{\partial n}$ the slope (shore-normal in our observations), and $|Q_{B,s}|(t)$ the alongshore transport component as computed using the Ribberink model. G is an efficiency factor dependent on the Shields number, the grain size and the presence of bed forms. For coarse sand and a Shields number below 0.5, $G \sim 1$ (Talmon & Wiesemann, 2006).

Lastly, the Ribberink model does not explicitly account for asymmetry driven transport. Orbital velocity asymmetry, close to but not identical to orbital acceleration skewness, leads to horizontal pressure gradients that might induce a net transport when the pressure gradients dominate the immersed weight of the grains (Sleath, 1999). Foster et al. (2006) observed asymmetry-driven incipient motion in the field at moments that the Sleath number ($Sw = \frac{\rho\sqrt{2}u_{rms}\omega}{(\rho_s - \rho)g}$ with $\omega = \frac{2\pi}{T_{m-1,0}}$ (Sleath, 1999)) exceeded a critical value of 0.29. Hoefel and Elgar (2003) added the contribution of acceleration skewed velocity forcing to an energetics model using the parameterization proposed from numerical experiments by Drake and Calantoni (2001):

$$Q_a = \text{sign}(a_{spike})K_a(|a_{spike}| - a_{crit}) \tag{10}$$

with $a_{spike} = \frac{\overline{a^3(t)}}{\overline{a^2(t)}}$, $a(t)$ the instantaneous acceleration signal, $^-$ time averaging over a relevant interval, K_a an efficiency coefficient set at 0.26×10^{-4} ms and a_{crit} a critical value of $\mathcal{O}1$ m/s^2. After recalibrating K_a to 1.4×10^{-4} ms and a_{crit} to 0.2 m/s^2 to fit the total net transport derived from observed bed level change to the

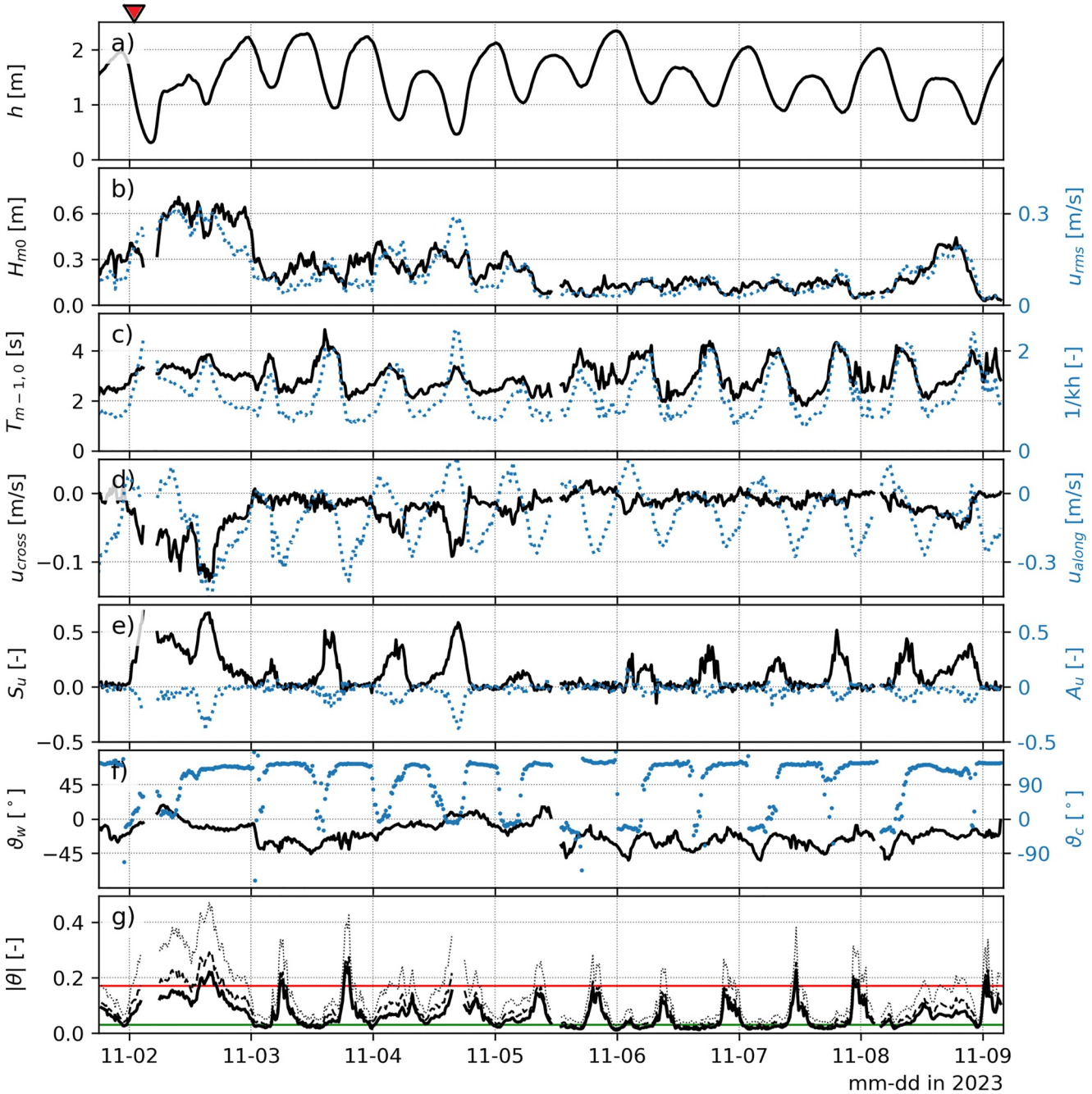

Figure 5. Hydrodynamics during the 7 day field campaign. Solid black lines correspond to the left *y*-axis, blue dotted lines correspond to the right *y*-axis. Values represent averages over 15-min intervals. (a) Water depth, (b) Significant wave height (black) and root-mean-squared orbital velocity (blue), (c) mean wave period (black) and relative water depth $\frac{1}{kh}$ (blue), (d) mean cross- (black) and alongshore (blue) velocity, (e) sea-swell orbital velocity skewness (black) and asymmetry (blue), (f) mean wave- (black) and current (blue) direction with respect to shore normal, (g) Block-representative magnitude of the Shields parameter (Equation 8): mean (solid line), root-mean-squared (dashed line) and 90% percentile (dotted line). Shields criterion for initiation of motion indicated in solid green, Shields criterion for onset of saltation in solid red. The triangular marker on top of panel a indicates the onset of the velocity profile measurements made by ACVP.

model, Hoefel and Elgar (2003) could capture both offshore as well as onshore bar migration, which was not possible without the acceleration skewness contribution Gallagher et al. (1998).

To compare the observed cross-shore ripple migration volumes with predicted cross-shore bed load transport, we averaged Equations 7, 9 and 10 over 15 min blocks. A log-modulus transformation (John & Draper, 1980) was

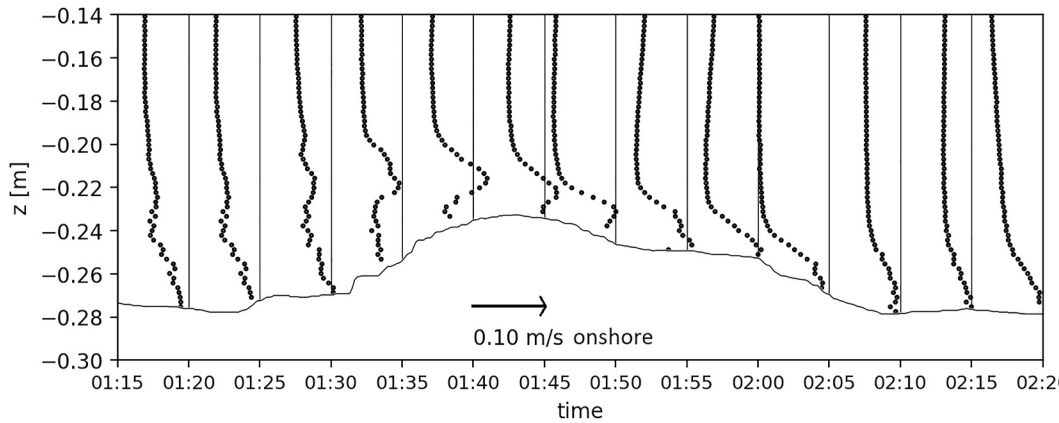

Figure 6. Measured near bed vertical profiles of time-averaged cross-shore velocity during shoreward migration of one ripple on 2023-11-02. 5-min averaged cross-shore flow velocity profiles from the ACVP data shown as black dots with respect to thin vertical axes. 5-min rolling averaged detected bed shown as the black solid line.

applied before comparing bed load predictions to the ripple volume transport to make transports spanning a few orders of magnitude including a sign change more comparable:

$$Q_b' = \text{sign}\left(10^6 \times Q_{B,cross}\right)\log\left(10^6 \times |Q_{B,cross}| + 1\right) \tag{11}$$

Note that Q_b' is dimensionless by scaling it to the dimensional unit of 10^{-6} m^2/s. This transformation is visualized in Figure 4.

3. Results

3.1. Waves and Currents

The hydrodynamic conditions over 7 days, beginning with storm Ciaràn on 11-02-2023 (November 2nd), are illustrated in Figure 5. Wave height peaked around 0.7 m during the storm, dropping to 0.35 m in the storm's aftermath and reducing even further to 0.2 m in the calm period between 11-05 and 11-08. The wave period during the storm was around 4 s, and was strongly modulated by the tide between 2 and 5 s in the post-storm period. Mean velocities in the cross-shore were up to 10 cm/s offshore during the storm, and mostly negligible after storm's passing. Alongshore velocities reached up to 50 cm/s during the storm, while in calm moments, in absence of wave-driven currents, tidal velocities were up to 30 cm/s. These calm moments show flood tidal current dominance of the flow field at the measurement location. Orbital velocity nonlinearity appears tidally modulated with S_u (A_u) values of just over 0.5 (-0.4) during the storm at low water, but returning to zero at high water levels each tide. Waves generally arrived obliquely from the south-east, apart from during the storm where waves arrived from the east. Tidal modulation is also apparent in the wave period and to a lesser extent in the significant wave height and the wave direction, which is a direct result of the subtidal shoal in front of the studied beach. The relative water depth ($0.8 < 1/kh < 2.5$) indicates intermediate water depths for the short-period waves, although water depth itself is shallow, ranging between 0.3 and 2.5 m, representative for low-energy field sites.

3.2. Near-Bed Velocity Field During Ripple Presence

An excerpt of 1 hr is extracted from the ACVP time series that captures the passing of one bed ripple in the onshore direction (Figure 6). Within the free-stream vertical range (e.g., 5 cm above the bed), 5-min averaged flow velocities were consistently offshore directed and weakly depth and time dependent. Near the bed, the mean flow over the ripple crest and on the seaward side reverses direction. At the crest of the ripple, the maximum onshore velocity is approximately 2 cm/s, while this profile's free-stream cross-shore velocity was 8 cm/s offshore directed.

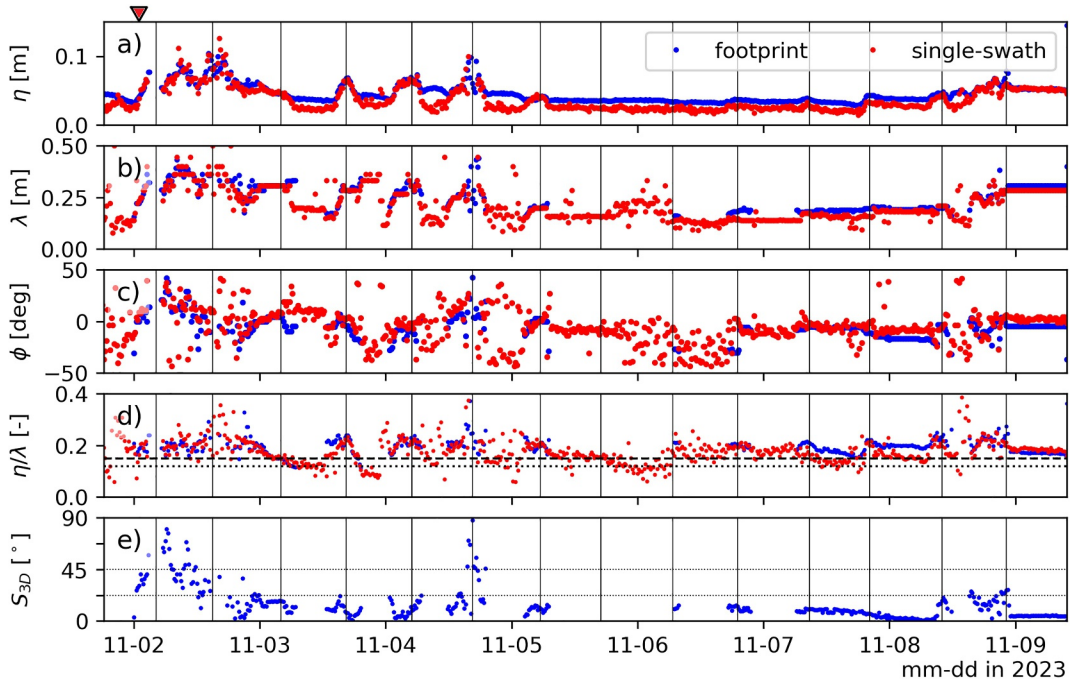

Figure 7. Timeseries of reconstructed ripple geometry. Extracted parameters are obtained through a 3D analysis of the entire footprint (blue) and by a 2D analysis of a single swath in the ripple direction (red). (a) Ripple height, (b) ripple wave length, (c) ripple direction with respect to shore normal, (d) ripple steepness. Black vertical lines show timing of semi-diurnal water level minima. Panel (d) also indicates the threshold steepness for vortex ripples (dotted black) and the generally predicted constant steepness of vortex ripples (dashed black line). (e) 3-Dimensionality parameter S_{3D}. The triangular marker on top of panel (a) indicates the onset of the velocity profile measurements made by ACVP.

3.3. Ripple Geometry

Ripple geometry from both 2D and 3D reconstruction is shown in Figure 7. Throughout the week, ripple height varied between 2 and 10 cm, ripple lengths between 0.1 and 0.4 m, ripple direction was predominantly shoreward oriented, varying from −45° to 45° obliquity to shore normal and ripple steepness varied between 0.1 and 0.3. Throughout the first 3 days, ripple geometry appeared to vary near-continuously; however, between 11-05 and 11-08 during low energy conditions (Figure 5), changes to ripple geometry only occurred during low tide (i.e., bedforms in the period between consecutive low tides appeared relic). The sensitivity of ripples to the water depth is most clearly evident in the ripple steepness that peaks at low tide and decreases in subsequent tidal phases (Figure 7d).

Geometric parameters derived from the 2D and 3D reconstruction methods are, for the most part, in good agreement. However, the 2D single-swath analysis did not resolve ripple variability in the along-ripple direction, and consequently resulted in a smaller ripple height than the 3D reconstruction. The alignment between the two methodologies during more energetic moments with low 3-dimensionality (Figure 7e) gives confidence that ripple height from the swath analysis correctly represents the ripple variance, while adding meaningful statistics in low-energetic conditions. Further analysis uses the 2D estimated ripple height and length.

Marking observations where ripple length was unchanged for more than 3 hr as relic, about 70% of the observations in our data classified as orbital ripples, whereas the other 30% were identified to be relic (Figure 8c). Recordings of relic ripple lengths appear above or left of the orbital ripple class in the diagram by Clifton and Dingler (1984) (Figure 8a) forming horizontal stripes of constant wave length with decreasing orbital excursion, similar to observations by Traykovski (2007). The observations that fall in the orbital ripple regime are reasonably predicted with the linear relation ($\lambda = 0.65 d_0$) between orbital excursion and ripple length according to Miller and Komar (1980) (Figure 8a). Given this relation holds for the majority of observations shows that orbital ripples are present at this site throughout a broad part of the surf zone. Nearly all (91%) of the observed orbital ripples

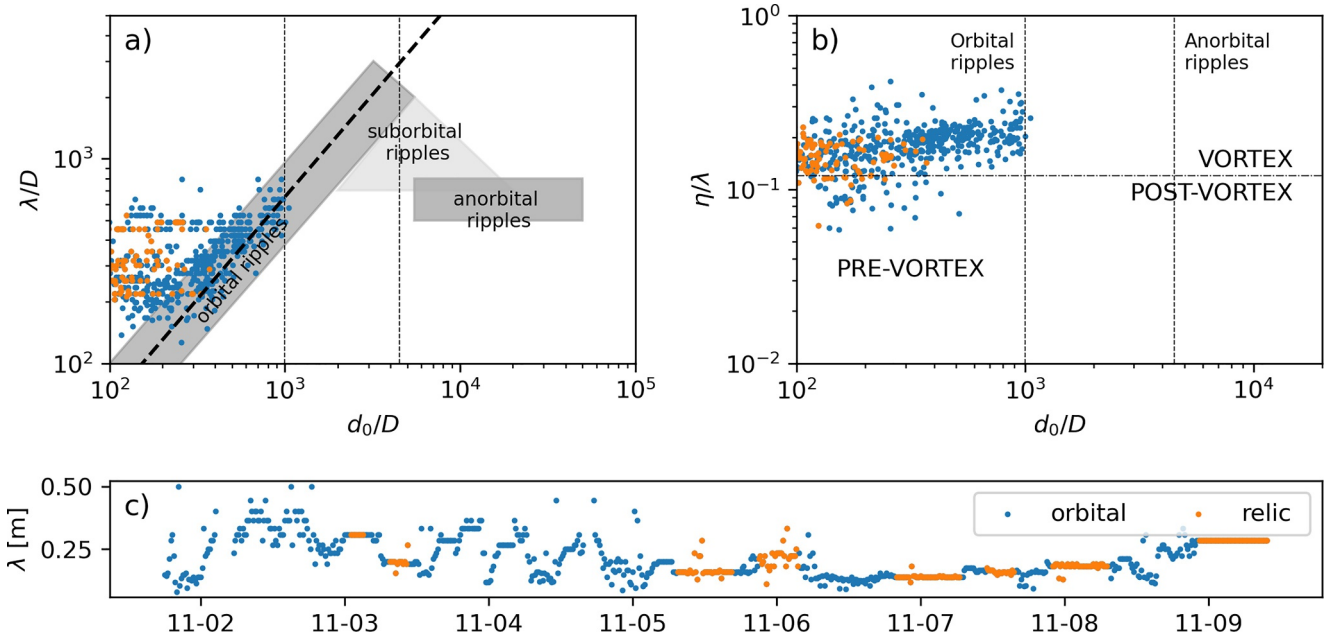

Figure 8. Observed ripple geometry placed within the classification scheme of Clifton and Dingler (1984). (a) Phase plane of ratio of ripple wave length to grain size versus ratio of orbital diameter to gain size, (b) Phase plane of ripple steepness versus ratio of orbital diameter to grain size. (c) Timeseries of ripple wave length. Marker color differentiates relic (orange) from orbital ripples (blue).

have a steepness that classifies them as vortex ripples (Figure 8b), with the remaining 9% interpreted as rolling-grain pre-vortex ripples. Of the relic ripples, 86% remained sufficiently steep to be classified as vortex ripples.

3.4. Migration

Ripple migration occurred very intermittently throughout the week (Figure 9). Between 11-03 12:00 and 11-05 06:00, ripples were alternatively migrating seaward or shoreward within a tidal cycle. During the calm period, ripples were stationary, with incidental small amounts of onshore migration. In the afternoon of 11-08, with increasing wave forcing, seaward and shoreward migration of ripples again occurred. During passing of the storm on 11-02, ripples were very steep, and the bed was very mobile, resulting in an interval of unresolved migration estimates due to large scan-to-scan variability.

A time stack of the central cross-shore swath shows that onset of migration occurred very rapidly (Figure 9a). Most times, the migration direction of individual ripples within this central swath was uniform over the cross-shore direction, apart from the migration event in the afternoon of 11-08. In general, some variation in the migration rates exists over the cross-shore direction.

The 2D migrate rate estimates were more sensitive to small migration rates, whereas the 3D estimates add value through showing the alongshore component that was of comparable magnitude as the cross-shore component. We evaluated a combined 2D-3D timeseries of cross-shore migration, where moments of missing 2D estimates of cross-shore ripple migration rate are replaced, when available, with the 3D estimate.

Ripple orientation was variable over time, ranging from −25° to 25° degrees oblique from shore-normal (Figure 9b). We tested whether the cross-shore migration rates could be explained through re-alignment of the ripple orientation. Ripple migration direction (Figure 9d) is not directly related to ripple orientation (Figure 9b); evidenced by a Spearman rank correlation between ripple direction and migration direction for all those observations with $|v_{mig}| > 1$ cm/hr of −0.07 at p-value of 0.4.

3.5. Drivers of Sediment Transport

The observed migration rates were rank correlated to the earlier identified potential driving mechanisms for bed load transport. Mean alongshore velocity correlates with the observed alongshore migration rate with a Spearman

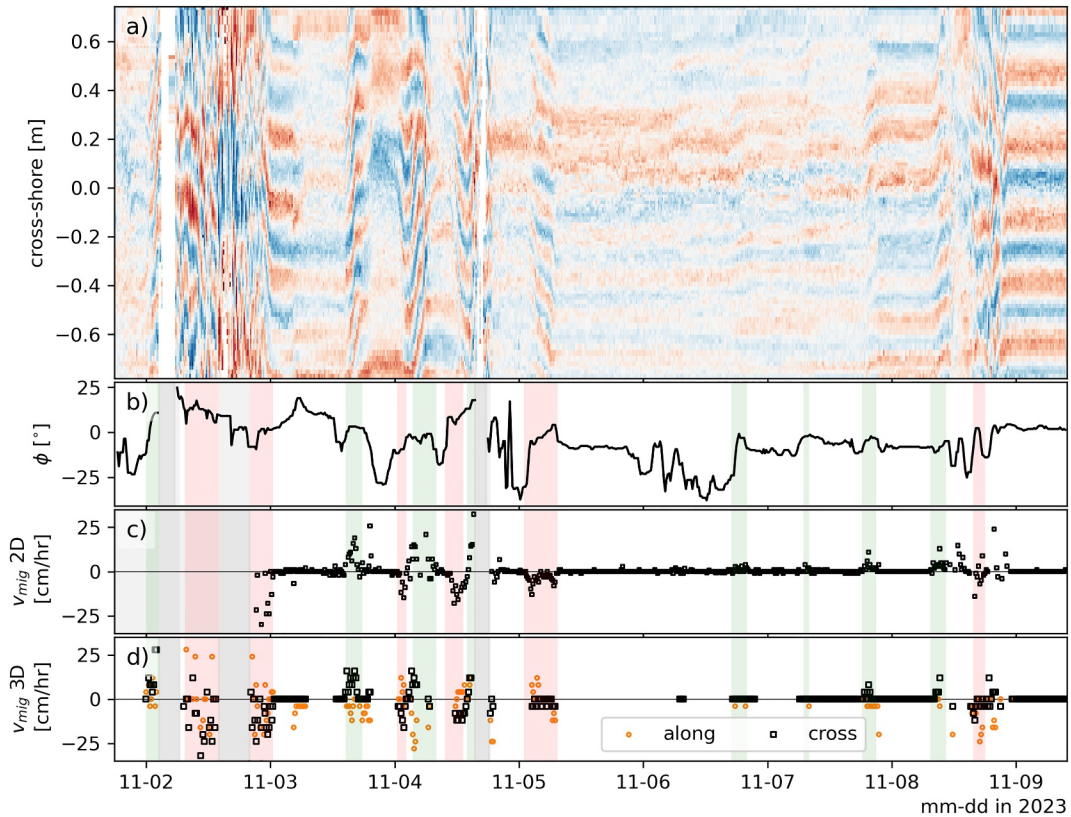

Figure 9. Observed ripple migration patterns. (a) Time stack of the detrended swath in the cross-shore direction. Ripple troughs in red, ripple crests in blue. (b) Ripple orientation with respect to shore-normal. (c) Estimated migration rate of the detrended swath in the ripple direction (from the 2D cross-correlation analysis) (d). Estimated migration rate from the 3D footprint analysis, both in cross-shore (black) and alongshore (orange) direction. Gray vertical bands in panel (b–d) indicate times with missing data. Vertical green (red) vertical bands in panels (b–d) refer to moments of shoreward (seaward) ripple migration.

rank correlation coefficient of 0.36 (p = 1e−11) in case all 699 15-min blocks of the data set are included (dof = n−2 = 697, with significance tested via an asymptotic t-approximation). During the 173 moments of observed alongshore migration (based on the condition $|v_{mig,cross}| > 1$ cm/hr) this rank correlation is 0.57 (p = 6e−13, based on an asymptotic t-approximation with dof = n−2 = 171), indicating that the mean alongshore flow clearly holds a relation with the alongshore component of ripple migration. In the cross-shore direction, the rank correlation between migration rate and mean cross-shore velocity is 0.08 (p = 0.05) (and increases to 0.16 (p = 0.03) in case moments with $|v_{mig,cross}| \leq 1$ cm/hr are excluded), showing that the relation therefore is weak (Figure 10b). The magnitude of the alongshore flow velocity, being the driver for downslope transport over transverse slopes, does not correlate to the observed cross-shore migration rate (r = 0.04, p = 0.4) when the entire timeseries is assessed. However, during moments of observed ripple migration this rank correlation is −0.17 (p = 0.02) which is still weak but does carry the correct sign (Figure 10c).

Wave nonlinearity is expected to drive cross-shore ripple migration. This is only evidenced weakly by the rank correlation computed over the entire timeseries (r = 0.11, p = 7e−3 in case of skewness and r = −0.20, p = 1e−6 in case of asymmetry), but this relation is clearer when compared for those moments with $|v_{mig,cross}| > 1$ cm/hr (r = 0.36, p = 2e−6 in case of skewness and r = −0.42, p = 1e−8 in case of asymmetry, Figures 10d and 10e). Observed wave shape has a consistent signature (positive valued S_u and negative valued A_u) that suggests an onshore contribution to ripple migration for both types of nonlinearity. As moments of nonzero S_u and A_u are also closely linked in time (Figure 5e), this analysis can't differentiate in the relative contribution of wave skewness-driven transport and wave asymmetry-driven transport.

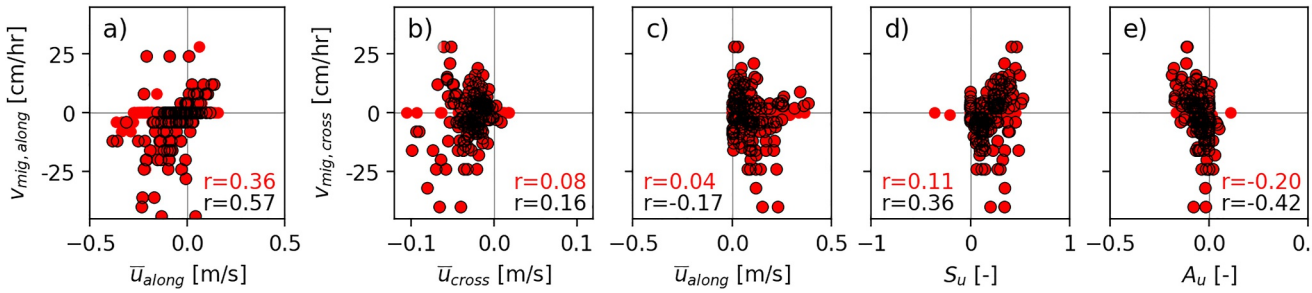

Figure 10. Relation between drivers of bed load transport and the observed alongshore and cross-shore ripple migration rates. Alongshore ripple migration rate versus (a) alongshore mean flow velocity, Cross-shore ripple migration rate versus (b), cross-shore mean flow velocity, (c) alongshore mean flow velocity, (d) orbital velocity skewness and (e) orbital velocity asymmetry. Red filled circles show all moments in the data set with corresponding Spearman rank correlation coefficient in red text. Black open circles show observations at moments of non-zero alongshore (a) or cross-shore migration rate (b–e) with corresponding Spearman rank correlation coefficient in black text.

The large discrepancy between rank correlations in- or excluding moments with $|v_{mig,cross}| <= 1$ indicates that the threshold of motion is an important aspect of the forcing balance. The fact that no single rank correlation explained more than half of the rank variance in the cross-shore migration rate indicates that the observed migration is a subtle interplay of the discussed mechanisms. To further unravel this balance their relative contribution will be compared in a quantitative approach using the proposed bed load transport predictor.

3.6. Bed Load Sediment Transport

The migration rates were converted into estimates of bed load transport using Equation 5 to compare them to quantitative bed load predictions. Over the week, the cross-shore ripple volume transport ranged from no movement at all up to 6.2e−6 m^2/s onshore and 5.8e−6 m^2/s offshore, which in dimensionless units Q_b' transforms to [−1.92, 1.98] (Equation 11 and Figure 11a).

The transport capacity of the horizontal pressure gradients is first examined. The Sleath number in our recordings did not exceed 0.11, suggesting that horizontal pressure gradients by themselves were not strong enough to initiate transport. That is not to say that horizontal pressure gradients could not contribute to bed load transport in the larger balance of forces once sediment is in motion by exceedance of the critical Shields parameter. The acceleration signal as derived from the cross-shore instantaneous velocity signal was used to compute a_{spike} (Equation 10) for all 15-min blocks. At all moments that a migration rate could be reconstructed, a_{spike} was positive, but lower than 0.18. This is lower than both values for a_{crit} proposed in literature (1 or 0.2), suggesting again that the horizontal pressure gradients are too weak to drive transport by themselves. In the three intervals that the cross-correlation between consecutive bed scans was too low to reconstruct a migration rate (vertical gray bands in Figures 9b–9d), a_{spike} reached up to 0.5, which is still below the critical value proposed by Drake and Calantoni (2001). Therefore, it is concluded that horizontal pressure gradients are an unlikely mechanism for the observed pattern of on- and offshore ripple volume transport. When sediment is already set in motion through other drivers, it could contribute, but only in the shoreward direction given the consistent positive sign of a_{spike}. Velocity asymmetry therefore acts in conjunction with the velocity skewness. The shear-stress driven component is investigated next, followed by an evaluation of the contribution of the gravity driven transverse bed slope effect.

Shear stress driven cross-shore sediment transport was quantified through Equation 6 with $\mathbf{u}(t)$, the total instantaneous velocity signal as input. This prediction shows moments with both onshore and offshore transport, of which some periods align with observed onshore migration. However, it strongly overpredicts transport in the offshore direction (Figure 11b). This was quantified by inter-comparing predicted bed load transport with the observed ripple volume transport (Figure 11g), excluding the times when reconstruction of the migration rate was not possible from this analysis (gray vertical bands in Figures 11a and 11b). The Spearman rank correlation coefficient was weak ($r = 0.19$, $p = 2e{-}6$) for the inter-comparison, with a large bias toward seaward directed transport, in particular at moments that no migration was observed. This is evidenced by the rank correlation improving to $r = 0.28$ ($p = 6e{-}4$) when computed only over those observations that cross-shore migration was observed ($|v_{mig,cross}| > 1$ m/s).

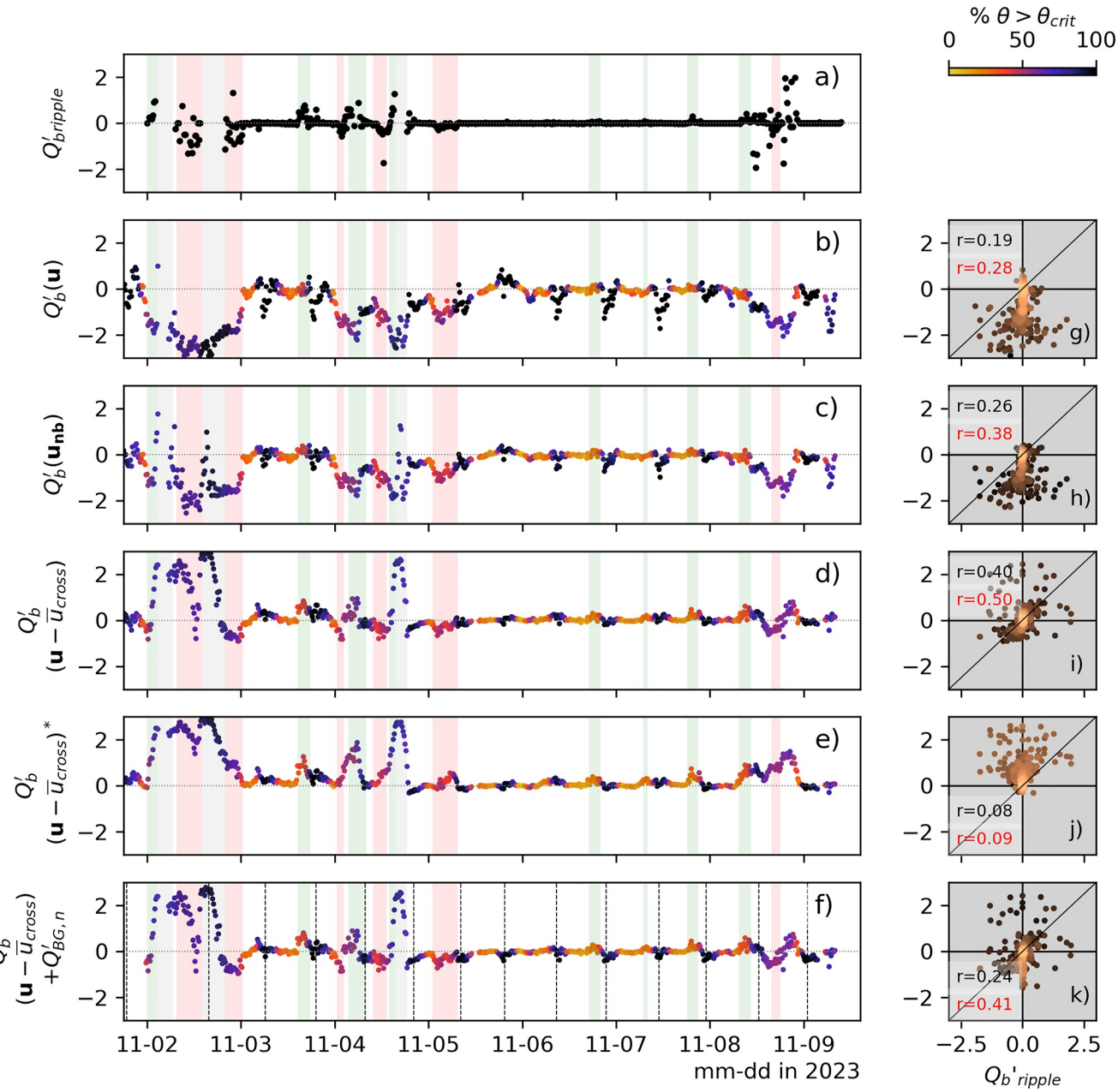

Figure 11. Comparing log-modulus transformed cross-shore bed load transport predictions using Equations 7 and 9 with the cross-shore ripple volume transport: (a) ripple volume transport, (b–e) bed load transport prediction with varying velocity components: (b) the full instantaneous velocity, (c) the instantaneous velocities with mean flow scaled to 2 cm above the bed, (d) the instantaneous velocities with cross-shore mean flow removed, (e) like panel (d) but with infragravity phase-angles replaced with random angles, (f) shear-stress induced transport as in panel (d) with gravity driven downslope transport according to Equation 9 added. Timeseries are color-coded with the percentage of samples within the 15 min blocks that exceed the threshold of motion θ_{crit}. Gray vertical bands indicate moments of missing migration rate estimates. Vertical green (red) vertical bands in Panels (a–f) refer to moments of shoreward (seaward) ripple migration. Vertical black dashed lines indicate local maxima in the alongshore flow magnitude in panel (f). Panels (g–k) show predicted transport magnitudes (y-axis) versus ripple volume transport (x-axis) corresponding with the timeseries in panels (b–f) respectively, with a Spearman rank correlation coefficient (computed over all observations (black) and over those with $|v_{mig,cross}| > 1$ m/s (red)) in the top left corner. Dots in these phase planes are colored on point-density for qualitative interpretation.

One cause of the overestimation of predicted bed load transport is the reduction in magnitude of free-stream mean flow in the boundary layer. Velocity profiles that resolve this attenuation were not available from the ACVP for the entire week, so the near-bed mean flow component at 5 cm above the bed ($\mathbf{u_{nb}}(t)$) was estimated using a simple logarithmic velocity profile (Hoekstra et al., 2004). Correction of this mean flow component to near-bed conditions changes the predicted net-sediment transport rate during the storm on 11-02, and reduces the

magnitude of offshore directed flow over the entire period (compare panels b and c in Figure 11). It also improves skill of the transport predictor ($r = 0.26$, $p = 3e{-}11$, Figure 11h). However, there is still a significant bias toward offshore directed transport, and there are numerous moments that offshore transport is predicted while no ripple volume transport was observed at all (predictions with black markers, Figure 11c, at moments of no observed ripple volume transport, Figure 11a). During these periods, the Shields parameter consistently exceeded the threshold of motion, whereas in other moments when ripple migration was observed (red and green vertical bands in Figure 11), the critical Shields threshold was exceeded for less than half of the block's duration (yellow to red markers, Figures 11b–11f). Therefore, Equation 6 forced with the total instantaneous velocity signal, both measured in the free-stream and near the bed, is a poor predictor of the observed ripple volume migration.

Both predictions including mean cross-shore current magnitude frequently overestimate critical shear stress exceedance and fail to accurately predict sediment transport direction. This indicates that not only the magnitude but also the direction of the mean current normal to the ripple crest in the free-stream is not representative of the near-bed conditions in this data set. This absence of correlation of the direction of cross-shore flow between free-stream and shear-stress driven bed load transport was also evidenced by a near-zero rank correlation between cross-shore mean flow velocity and observed cross-shore migration rate (Figure 10b). Supporting evidence was provided by the 2 hr of ACVP data, which revealed that the net flow direction measured up to 5 cm above the ripple surface can diverge from that of the free-stream flow on the ripple crest (Figure 6). Therefore, the skill of a wave-driven bed load predictor ignoring the cross-shore component of the mean flow, that is, de return flow, in the free stream was evaluated as well, by applying Equation 6 to $\mathbf{u_{nb}} = [u_{cross} - \overline{u_{cross}}, u_{along}]$ (Figure 11d).

In this case, all but one (11-02 10:30) of the identified moments of ripple migration were predicted with the correct sign (onshore or offshore, Figure 11d, with $r = 0.40$, $p = 1e{-}24$). The rank correlation for this case also improves in case it is computed only over moments of observed migration, but to a lesser extent (to 0.50, $p = 1e{-}10$). This shows that orbital velocities can drive a net transport, potentially through interactions between different frequency components in the velocity signal.

It is furthermore insightful to visualize the transport predicted in case the phase-information in the infragravity frequency range is replaced with random angles: $\mathbf{u^*_{nb}} = [u_{cross} - \overline{u_{cross}}, u_{nb,along}]^*$. The IG frequency range includes all variance at frequencies below $f_p/2$. During moments of migration, the variance of $u_{cross,ig}$ never exceeded 10% of the total variance in u_{cross}, suggesting that these wave lengths by themselves do not hold transport capacity. By replacing the observed IG phase-angles with random angles and then recomputing the bed load prediction, repeating this 50 times and averaging the outcome, it is tested to what extent phase-coupling between IG frequencies and sea-swell frequencies contributes to the predicted transport directions.

With replacement of IG angles with random phase-angles, the bed load model solely predicted onshore transport, thereby diminishing the Spearman rank correlation to $r = 0.08$, $p = 0.04$ (Figures 11e and 11j). This evidences that there exists phase-coupling of infragravity and sea-swell velocity variance at moments that the critical Shields threshold was exceeded. The phase-information in the infragravity frequency band appears to be essential to replicate moments of offshore directed ripple volume transport (comparing Figure 11d with Figure 11e).

Downslope transport due to alongshore mean flow over the bed slope could be an alternative driving mechanism for offshore transport. The magnitude of this contribution was added to the shear-stress driven transport to explore this in Figures 11f and 11k. The combined model (Equations 7 and 9) had a lower rank correlation with the observations ($r = 0.24$, $p = 9e{-}10$) than the shear-stress only model. Moments of observed ripple migration did not coincide with local alongshore velocity maxima, whereas the predicted alongshore transport and thereby the gravity driven cross-shore transport did. The addition of the transverse bed slope effect adds negative bias to the model at moments without observed ripple migration, while at the same time it did not show different contributions to the moments of on- and offshore migration. Therefore, the gravity-driven bed slope effect was not a driving mechanism for the observed cross-shore ripple volume migration.

4. Discussion

4.1. Relating Ripple Migration to Bed Load Transport Direction

It need not always be the case that the ripple migration pattern is equal to the net sediment transport direction. For example, dunes in river beds have been observed to migrate upstream in the case of supercritical flow (e.

g., Núñez-González & Martín-Vide, 2011). The Froude number in our observations remains well below 1 ($F = \frac{u_r ms}{\sqrt{gh}} \leq 0.2$ in the entire data set), which rules out a similar process ongoing here. Alternatively, a phase shift between suspension/saltation and deposition under asymmetric orbital wave forcing can lead to a net total transport direction that is different from the ripple migration direction. In such a scenario, the migration rate of the ripples will also hold a weak relation or no relation at all to the magnitude of the bed load transport (e.g., Ribberink et al., 2008). This scenario is unlikely for this data set as the Shields parameter indicates that transport is mostly in the bed load regime, particularly at all but one moment of observed ripple migration the mean Shields parameter did not exceed 0.17, the threshold for saltation as suggested by Amos et al. (1999) (combine Figure 5g with Figures 9c and 9d). The low-energy forcing and coarse grain size therefore rule out the hypothesis of opposing net directions between ripple volume transport and bed load transport.

4.2. Phase Coupling as a Driving Mechanism

Including the infragravity frequencies and its phase-information in the bed load transport model proved necessary to reproduce moments of offshore migration 4.6 and its relevance was attributed to phase-coupling between sea-swell frequencies with infragravity frequencies. This phase coupling can be shown more explicitly by inspecting the normalized magnitude of the bispectrum and its phase. We computed bicoherence spectra $b(f,f)$ from near-bed pressure (as recorded by the ADV) following the definition of Haubrich (1965). The bispectra were calculated over 1-hr timeseries, divided into blocks of 300 s with 50% overlap, combined with frequency merging to increase the statistical stability, resulting in a 95% significance level for zero bicoherence of 0.14 (Elgar & Guza, 1988). The bicoherence spectrum can be divided into four zones (de Bakker et al., 2015): Zone I contains infragravity frequencies only, zone II contains two infragravity and one short-wave frequency, zone III contains two short-wave and one infragravity frequency, and zone IV contains short-wave frequencies only, see Figures 12b–12g. Here, we are interested in phase coupling in zone III.

Bicoherence in zone III was usually statistically significant ($b > 0.14$) at moments of observed ripple migration, both in onshore and offshore direction. During calm conditions with a stationary bed, the bicoherence values were generally lower than the significance threshold. Example bicoherence and phase of three moments of ripple migration are shown in Figures 12b, 12d, and 12f. For those triad-interactions that the bicoherence was significantly different from zero, the biphase is also shown (Figures 12c, 12e, and 12g). These phase spectra show that the coupled infragravity frequency is out of phase with the sea-swell frequencies involved in zone III which is consistent with the observed phase coupling inferred from averaging Equation 7 in- or excluding the phase-angles of the IG band in Section 3.6, thus showing the contribution of the infragravity waves to offshore sediment transport.

Our study is not the first to conclude that orbital velocity components best prescribe the ripple volume transport direction and that infragravity components should be included. Crawford and Hay (2001) concluded that the direction of ripple migration can be estimated best with the oscillating component of the free-stream velocity signal and that they need both gravity and infragravity components of the orbital components to properly explain the migration direction. The hydrodynamic forcing studied in Crawford and Hay (2001) was much more energetic than the conditions we discussed; their observations were close to the sheet-flow transition, with ripples in the anorbital regime, while our observations just exceed the threshold of motion and ripples are in the orbital-vortex regime.

4.3. Role of Mean Flow in Bed Load Transport on Top of Vortex Ripples

Doucette (2002) (D2002) and Miles et al. (2014) (M2014) suggested that ripple migration direction in their data set was a balance between undertow and orbital velocity skewness. The observed ripple volume transport in our data set was not well represented with a bed load model including the measured mean flow. This could be due to the fact that mean flow conditions were particularly weak in our data set with coarse-grained vortex ripples, such that near-bed streaming velocities due to wave processes will exceed the influence of the return current in the free-stream on true bed load transport. Cross-shore mean flow velocities in D2002 and M2014 were in fact comparable to our data set, ranging 4–8 cm/s in D2002 and 2–15 cm/s in M2014. Unlike our data set however, the transport regime, indicated by the Shields parameter, in these works consistently indicated saltation and/or suspended transport (θ always above 0.2, and averaging 0.5 in M2014, mostly due to the finer sediment, and between 0.26 and 0.6 during moments of migration in D2002, mostly due to wave forcing of much larger wave period).

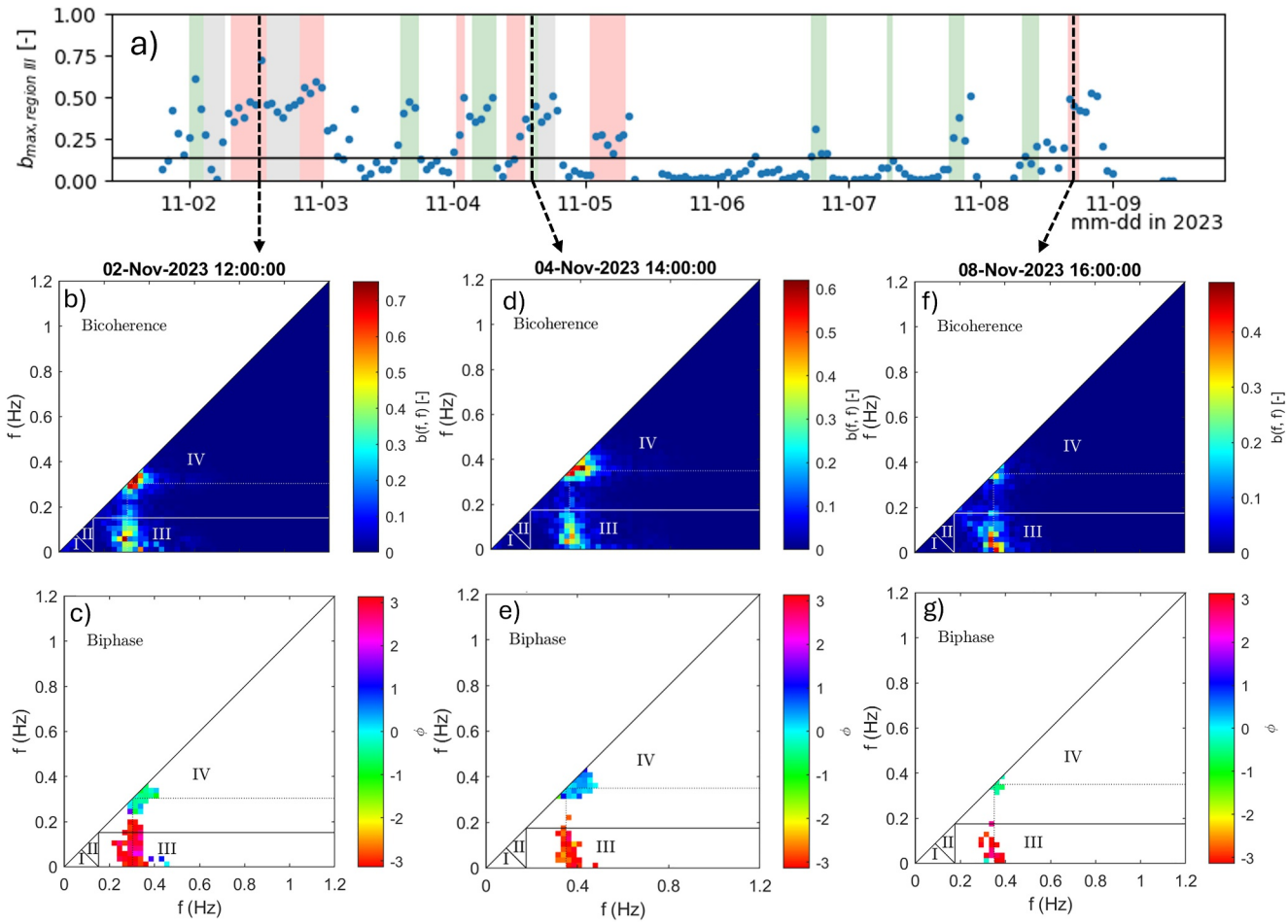

Figure 12. Timeseries of the maximum bicoherence at frequencies in zone III (a) together with three bicoherence spectra (b, d, f) with corresponding phase spectra (c, e, g) taken at moments of observed ripple migration. White (black) lines in panels b, d, f (c, e, g) demarcate the interaction zones as discussed in de Bakker et al. (2015), with zone III notable for interactions involving two sea-swell frequencies and one infragravity frequency.

Sediment transport in suspension or saltation will be more strongly affected by the return current. The one moment of offshore ripple migration that our model could not capture on 11-02 around midday, was also the migration moment with the largest 15-min averaged Shields parameter $\theta = 0.15$ (Figure 5g). This is close to a Shields value of 0.17 that we adhere to as the threshold for saltation (e.g., Amos et al., 1999). The apparent discrepancy in conclusion can therefore be attributed to a difference in the transport regime under which the ripple migration is studied.

Another clarification of the diverging findings between different studies can be the difference in sediment composition. Cummings et al. (2009) show that vortex ripples develop much more prominently for coarse-grained sand than for fine-grained sand. Therefore, mean flow might affect the migration direction of fine-grained suborbital/anorbital post-vortex ripples, while during coarse sand experiments (such as ours) the mean flow direction might be unrelated to wave bottom boundary layer mean flow velocities because of the presence of steep bed ripples.

4.4. Processes Affecting the Near-Bed Flow Field Over the Ripple Surface

In previous field experiments ripple migration has been successfully related to the free-stream return flow as a proxy for the WBBL flow (D2002, M2014). For the current field experiment we find that the cross-shore free-stream velocity has no predictive skill for the WBBL flow direction. This is not a new finding and has been observed in several laboratory experiments (e.g., Bijker et al., 1974; Marin, 2004). This is now supported for the first time with our field observations showing that the WBBL flow direction on top of vortex ripples is

decorrelated from the free stream in a real sea-state with oblique ambient tidal currents present. This contradictory finding can be explained by the balance between different contributions to WBBL flow.

The net flow direction within the wave bottom boundary layer (WBBL) on a flat bed is the superposition of return flow (as a result of horizontal pressure gradients, also present in the measurements at 30 cm above the bed), progressive wave streaming (Longuet-Higgins, 1953), not measurable above the wave bottom boundary layer, and wave shape streaming (Davies & Villaret, 1999; Kranenburg et al., 2012). These processes can alter the net flow direction in the WBBL, as modeled by Kranenburg et al. (2013) and observed in the lab by Schretlen (2012) for a range of nonlinear forcings, but this need not always be the case (Van Der Zanden et al., 2017). On a rippled bed, the effect of both streaming mechanisms will be dampened by the experienced rugosity of the ripples, but another component to the mean flow might be added. Orbital motions around the ripples can generate vortices that are ejected into the water column at flow reversal which may result in mean flow patterns depending on differences in vorticity at on- and offshore flow reversal due to velocity nonlinearity (DeVoe et al., 2025; Fritsch et al., 2024; Yuan, 2023). Our analysis does not elucidate which of these mechanisms is most dominant, but it does confirm that in our data set, near-bed velocities above the rippled bed are uncorrelated to the free-stream mean flow conditions.

4.5. Unresolved Variance

Although all but one moment of ripple migration direction are predicted accurately, the Spearman rank correlation of the most descriptive bed load model is only 0.4 (Figure 11j), indicating that the majority of the rank variance is left unexplained $\left(r^2 = 0.16\right)$. This can partly be explained by an over-representation of moments of near-zero bed load transport with near-zero predicted bed load transport that are assigned a somewhat arbitrary rank in comparison to the ranks assigned to moments with observable on- or offshore bed load transport. Excluding the moments with no observed cross-shore migration, the rank correlation improved slightly to 0.5 $\left(r^2 = 0.25\right)$. Still, the majority of scatter in the model-data comparison remains unexplained. This shows that the Ribberink model does not have much predictive skill in describing our observed ripple volume transport on the 15-min resolution over the entire campaign period.

The bed load model is however useful in confirming what balance of driving processes can explain the observed transport directions. Moreover, it helped show that the cross-shore component of the mean flow measured in the free stream did not have predictive skill, even when assessed in balance with other drivers. This conclusion is likely particular to the transport regime we observed very close to initiation-of-motion ($\theta < 0.15$ on top of vortex ripples), and with weak but non-zero return flow magnitudes.

The limited predictive skill here might also reflect a limitation in this bed load model. The Ribberink model uses a block-averaged wave friction factor, whereas in reality, the friction factor will be varying over the intrawave time scale (Trowbridge & Lentz, 2018). The 15-min block average wave friction factor should not only be affected by the sea-swell contribution included in the formulation used by Swart (1974), but also be affected by the mean flow and IG contributions. Phase-averaged theories exist that weigh the wave- and the current contribution to the block-averaged wave friction factor, but these are unsuitable for a bedload prediction based on instantaneous velocity signals and do not account for the infragravity band (e.g., Grant & Madsen, 1979; Soulsby, 1997). Comprehensive theories integrating the effects of mean currents, IG and sea-swell contributions on the friction factor are necessary to further improve bed load predictions of the observed ripple volume transport.

5. Conclusions

This study presents field observations of vortex ripples and their migration from a low-energy beach composed of coarse sediment ($D = 630$ μm) using a Sand Ripple Profile Scanner on footprints of 1.5 m diameter. Shields parameter values (15-min averages always < 0.2, and always below < 0.15 during moments of observed ripple migration) indicated bed load was the dominant mode of sediment transport. The bed load transport associated with ripple migration was shown to be highly intermittent, while the bed was continuously rippled, with relic and orbital vortex ripples. Both moments of seaward and shoreward ripple migration were recorded.

The alongshore component of the observed ripple migration correlated with alongshore mean velocity which was largely driven by the tide, whereas cross-shore migration showed no correlation with cross-shore mean velocity which was driven by a wave-induced return current. Our observations of the mean cross-shore velocity profile

above a shoreward migrating vortex ripple confirm that near-bed cross-shore velocity recordings, even as close as 5 cm above the vortex ripple crests, need not capture the mean current direction in the wave bottom boundary layer.

We investigated to what extent the direction of cross-shore bed load transport associated with the ripple migration could be understood from free-stream velocity observations. A bed load sediment transport model forced with the total measured free-stream velocity signal led to a consistent over-prediction of offshore directed transport, including prediction of offshore transport at moments that the rippled bed was at rest and no bed load transport was observed. Using only the measured oscillating velocity components ($u_{rms} < 0.3$ m/s), thus excluding the mean cross-shore velocity ($\overline{u_c} < 0.1$ m/s), the bed load model captured the correct direction of all but one observed instance of migration. Although the variance in the infragravity band of the velocity signal was small ($< 10\%$) compared to the incident band, it proved crucial to include this band in the forcing of the transport model to differentiate onshore from offshore moments. In the model, when the phase information in this band was replaced with random angles, the model only predicted bed load transport in onshore direction.

This analysis highlights that the bed load transport direction over coarse-grained vortex ripples during low-energy and directional wave-current forcing is a balance between both super- and subharmonic wave components that can be observed within the free-stream.

Appendix A: Ripple Geometry Reconstruction

Both approaches to reconstruct the ripple geometry started with detection of the bed level in the echogram of each individual sonar swath by exploiting the fact that in our data set the backscatter intensity saturated on the bed over a radial range of about 4 cm. For each of the 200 swaths in one scan, backscatter intensity was first converted into a binary signal equal to 1 in case the saturation limit was reached and equal to 0 when it was below the saturation limit. Then, a moving average was applied to the binarized swath over 15 cells in the radial direction and 15 cells in the arc-direction. For each ping in the swath, the interface between the fluid and the bed was set at the maximum of this moving averaged binarized backscatter signal (Figure A1a).

For the 3D geometry characterization, bed level data from all swaths was combined by linear Loess interpolation (Plant et al., 2002) from polar coordinates onto a regular Cartesian 1×1 m grid with 1×1 cm resolution (which approximates the intrinsic resolution of the raw data at 75 cm below the sonar head in the nadir). The footprint was linearly detrended to remove beach slope, after which η_{3D} was estimated as $\eta_{3D} = 4\sqrt{\langle z_b - \langle z_b \rangle \rangle^2}$ excluding any missing z_b values (e.g., Traykovski, 2007; Wengrove et al., 2017). Then, any missing values were filled with the mean ($z_b = 0$), after which a variance preserving Hamming window was applied on the footprint (Figure A1b). The result was then transformed into wavenumber space using a 2DFFT, in which we artificially enhanced the wavenumber resolution from $\Delta k = 1$ m^{-1} to $\Delta k = 0.25$ m^{-1} by zero-padding the footprint in each direction to increase the surface area by a factor 16. This does not add physical resolution to the image (e.g., does not help to de-alias two peaks spaced less than $\Delta k = 1$ m^{-1} apart, as the intrinsic resolution of the footprint, 1 cm $\times$ 1 cm, does not change), but aids the differentiation between 0.3 and 0.4 m peak ripple wave lengths, which would otherwise end up in the same wavenumber bin (of $k = 3$ m^{-1}) and instead fall in the wavenumber bins $k = 3.25$ m^{-1} and $k = 2.5$ m^{-1}. The peak of the wavenumber spectrum was then identified over the positive y-axis half-plane, where variance with a wavenumber $|\mathbf{k}| = \sqrt{k_{cross}^2 + k_{along}^2} < 2$ was removed to avoid the extraction of ripple lengths that fit less than twice in the cropped footprint (Figure A1c).

From the peak wavenumber, λ_{3D} was estimated as $\frac{1}{\sqrt{k_{cross}^2 + k_{along}^2}}$ and the ripple orientation as $\psi_{3D} = \tan^{-1}(k_{along}/k_{cross})$. In case the estimated peak wavenumber $|k|$ was 2 m^{-1} (e.g., exactly on the edge of the removed variance density cut), λ_{3D} was set to NaN, as the large scale curvature of the bed could not be separated from the bed forms.

Lastly, for each of the recordings, we computed a measure of 3-dimensionality of the ripple structure from a principal component analysis (PCA) of the bed level variance. Here, the principle axis was set in the peak-ripple direction and the secondary axis was set orthogonal to this. Variance in these two axes was related to a spreading parameter computed as $S_{3D} = \tan^{-1}(\text{var}_2/\text{var}_1)$ with var_2 and var_1, the variance in secondary and principal direction respectively. Spreading values are bound between [0, 90]°. Larger spreading values indicate a more

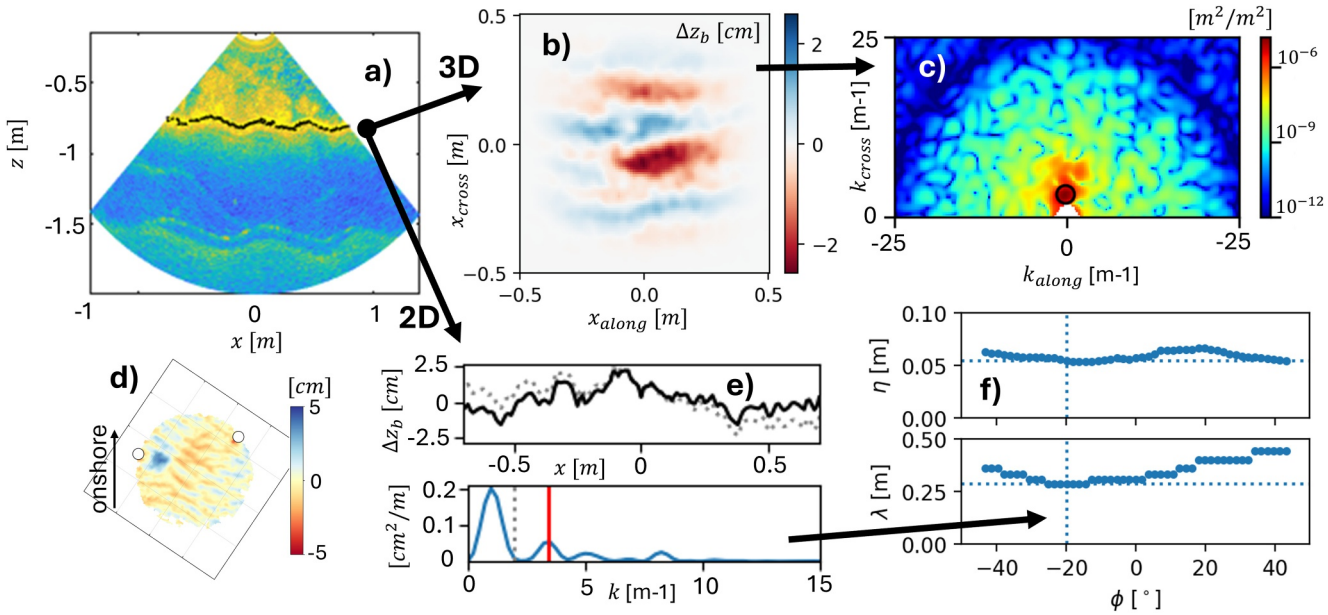

Figure A1. Outline of reconstruction of ripple geometry through 3D footprint analysis (a–c) or 2D single-swath analysis (a, d–f). (a) Detected bed level (black dots) on top of the raw backscatter intensity of an individual swath. Yellow (blue) colors represent high (low) backscatter intensity, (b) detrended and windowed bed level footprint after interpolation of all swaths in a circular scan to regular grid, (c) cropped 2D wavenumber power spectrum over the positive cross-shore half-plane with the peak wavenumber identified by the black open circle. (d) example footprint with sediment deposited in wake of frame's pole, (e) bed level of an individual swath (gray dashed line—mean depth removed, black—linearly detrended) and its cropped 1D wavenumber power spectrum of an individual detrended swath, with peak wave length identified as first peak larger than 2 m^{-1} (red line), (f) ripple height and wave length as function of swath angle with respect to shore normal. Selection of scan's peak ripple length and wave height based on the angle that minimizes the ripple length (blue dotted vertical and horizontal lines).

3-dimensional structure, but as long as values remain below 45° the variance in the peak ripple direction exceeds the secondary axis. Values above 45° indicate that organized ripples are not dominating the bed level variance.

In the second approach, adjacent swaths were moving-averaged using a 5-step window. These smoothened swaths were then linearly detrended to remove beach slope on an individual basis to reconstruct ripple length and height from a 1D FFT (Figure A1e). The peak wavenumber larger than 2 m^{-1} was associated to the swath's ripple wave length $\left(\lambda = \frac{2\pi}{k_p}\right)$. The orientation of the swath with minimum reconstructed ripple length was then set as the ripple direction (ϕ_{2D}). Ripple height η_{2D} and length λ_{2D} from this particular swath were set as this scan's 2D-estimate of geometry (Figure A1f).

Migration speed and direction were based on the peak of the correlogram of two subsequent scans as $v_{mig} = \frac{1}{\Delta t}\sqrt{x_p^2 + y_p^2}$ and $\phi_{mig} = \tan^{-1}(y_p/x_p)$, where $\Delta t = 15$ min is the time between the subsequent scans. The migration rate was then decomposed in a component cross-shore (v_{cross}) and a component along-shore (v_{along}). Times with scan-to-scan peak cross-correlation below 0.5 were discarded, as well as times that the ripple geometry could not be resolved from the 23D approach.

Similarly, ripple migration in the ripple direction was estimated from the 5-window moving averaged swaths from the 2D approach using a 1D cross-correlation. To artificially increase the resolution of the 2D migration rate estimates, the swath in ripple direction was first interpolated onto a 25 cm resolution grid, which results in 4 times more resolution in migration rate estimates than extracted from the footprint approach. These 2D estimates of migration rate (v_{2D}) were then projected in the cross-shore direction through $v_{cross,2D} = \cos(\phi)v_{2D}$. In this approach, moments with scan-to-scan peak cross-correlation below 0.7 were discarded. The mean cross-correlation of the remaining migration rate estimates was 0.93.

Conflict of Interest

The authors declare no conflicts of interest relevant to this study.

Availability Statement

Data and python scripts underlying the analysis and figures of this research are published in the 4TU repository at https://doi.org/10.4121/ad1ad426-3c19-43a1-a4b6-c726426bc53a (Van Der Lugt et al., 2026).

Acknowledgments
Thanks to the anonymous reviewers whose suggestions greatly improved this manuscript. Many thanks go to MSc students Floris van Dijk and Daan Koets and to lab technicians Pieter van der Gaag and Arie van der Vlies for their initiative and hard work that made this field campaign possible. We thank Ubertone for development of the prototype UBFlow-3c used for this research and Guillaume Fromant for his contribution on conception and design of the UBFlow-3c and scripts to debinarize the ACVP data stream. This work is part of the research program: EURECCA "Effective Upgrades and REtrofits for Coastal Climate Adaptation" under project number 18035, financed by NWO Domain Applied and Engineering Sciences. NF and FF were funded through ANR project WEST (ANR-20-CE01-0009) and NF through IsBlue mobility Grant (ANR-17-EURE-0015) for her research visit to the Netherlands.

References

Amos, C., Bowen, A., Huntley, D., Judge, J., & Lit, M. (1999). Ripple migration and sand transport under quasi-orthogonal combined flows on the Scotian Shelf. *Journal of Coastal Research*, *15*, 1–14.

Andersen, K. (1999). *Ripples beneath surface waves and topics in shell models of turbulence* (PhD thesis). Technical University of Denmark, Department of Hydrodynamics and Water Resources (ISVA).

Austin, M. J., Masselink, G., O'Hare, T. J., & Russell, P. E. (2007). Relaxation time effects of wave ripples on tidal beaches. *Geophysical Research Letters*, *34*(16), 2007GL030696. https://doi.org/10.1029/2007GL030696

Bagnold, R. (1946). Motion of waves in shallow water. Interaction between waves and sand bottoms. *Proceedings of the Royal Society of London - Series A: Mathematical and Physical Sciences*, *187*(1008), 1–18. https://doi.org/10.1098/rspa.1946.0062

Becker, J. M., Firing, Y. L., Aucan, J., Holman, R., Merrifield, M., & Pawlak, G. (2007). Video-based observations of nearshore sand ripples and ripple migration. *Journal of Geophysical Research*, *112*(C1), 2005JC003451. https://doi.org/10.1029/2005JC003451

Bijker, E. W., Kalkwijk, J. P. T., & Pieters, T. (1974). Mass transport in gravity waves on a sloping bottom. *Coastal Engineering*, *1974*, 447–465.

Brinkkemper, J. A., Aagaard, T., de Bakker, A. T. M., & Ruessink, B. G. (2018). Shortwave sand transport in the shallow surf zone. *Journal of Geophysical Research: Earth Surface*, *123*(5), 1145–1159. https://doi.org/10.1029/2017JF004425

Cizek, V. (1970). Discrete Hilbert transform. *IEEE Transactions on Audio and Electroacoustics*, *18*(4), 340–343. https://doi.org/10.1109/TAU.1970.1162139

Clifton, H. E., & Dingler, J. R. (1984). Wave-formed structures and paleoenvironmental reconstruction. *Marine Geology*, *60*, 165–198.

Costas, S., Alejo, I., Vila-Concejo, A., & Nombela, M. A. (2005). Persistence of storm-induced morphology on a modal low-energy beach: A case study from NW-Iberian Peninsula. *Marine Geology*, *224*(1–4), 43–56. https://doi.org/10.1016/j.margeo.2005.08.003

Crawford, A. M., & Hay, A. E. (2001). Linear transition ripple migration and wave orbital velocity skewness: Observations. *Journal of Geophysical Research*, *106*(C7), 14113–14128. https://doi.org/10.1029/2000JC000612

Cummings, D. I., Dumas, S., & Dalrymple, R. W. (2009). Fine-grained versus coarse-grained wave ripples generated experimentally under large-scale oscillatory flow. *Journal of Sedimentary Research*, *79*(2), 83–93. https://doi.org/10.2110/jsr.2009.012

Davies, A. G., & Villaret, C. (1999). Eulerian drift induced by progressive waves above rippled and very rough beds. *Journal of Geophysical Research*, *104*(C1), 1465–1488. https://doi.org/10.1029/1998JC900016

De Bakker, A. T. M., Brinkkemper, J. A., Van Der Steen, F., Tissier, M. F. S., & Ruessink, B. G. (2016). Cross-shore sand transport by infragravity waves as a function of beach steepness. *Journal of Geophysical Research: Earth Surface*, *121*(10), 1786–1799. https://doi.org/10.1002/2016JF003878

de Bakker, A. T. M., Herbers, T. H. C., Smit, P. B., Tissier, M. F. S., & Ruessink, B. G. (2015). Nonlinear infragravity–wave interactions on a gently sloping laboratory beach. *Journal of Physical Oceanography*, *45*(2), 589–605. https://doi.org/10.1175/JPO-D-14-0186.1

DeVoe, S. R., Wengrove, M. E., Foster, D. L., & Hagan, D. S. (2025). Characterization of the spatiotemporal distribution of shear stress and bedload flux within a mobile, rippled bed. *Journal of Geophysical Research: Oceans*, *130*(9), e2025JC022369. https://doi.org/10.1029/2025JC022369

Dey, S. (2003). Threshold of sediment motion on combined transverse and longitudinal sloping beds. *Journal of Hydraulic Research*, *41*(4), 405–415. https://doi.org/10.1080/00221680309499985

Doucette, J. (2002). Bedform migration and sediment dynamics in the nearshore of a low-energy Sandy beach in Southwestern Australia. *Journal of Coastal Research*, *18*, 576–591.

Drake, T. G., & Calantoni, J. (2001). Discrete particle model for sheet flow sediment transport in the nearshore. *Journal of Geophysical Research*, *106*(C9), 19859–19868. https://doi.org/10.1029/2000JC000611

Elgar, S., & Guza, R. (1988). Statistics of bicoherence. *IEEE Transactions on Acoustics, Speech, and Signal Processing*, *36*(10), 1667–1668. https://doi.org/10.1109/29.7555

Fernandez Luque, R., & Van Beek, R. (1976). Erosion and transport of bed-load sediment. *Journal of Hydraulic Research*, *14*(2), 127–144. https://doi.org/10.1080/00221687609499677

Foster, D. L., Beach, R. A., & Holman, R. A. (2006). Turbulence observations of the nearshore wave bottom boundary layer. *Journal of Geophysical Research*, *111*(C4), 2004JC002838. https://doi.org/10.1029/2004JC002838

Frank-Gilchrist, D. P., Penko, A. M., Palmsten, M. L., & Calantoni, J. (2024). Vortex trapping of suspended sand grains over ripples. *Journal of Geophysical Research: Earth Surface*, *129*(10), e2023JF007620. https://doi.org/10.1029/2023JF007620

Fritsch, N., Floc'h, F., & Fromant, G. O. Y. (2026). In situ observations of wave boundary layer hydrodynamics in the surf and shoaling zones.

Fritsch, N., Fromant, G., Hurther, D., & Cáceres, I. (2024). Coarse sand transport processes in the ripple vortex regime under asymmetric nearshore waves. *Journal of Geophysical Research: Oceans*, *129*(4), e2023JC020189. https://doi.org/10.1029/2023JC020189

Gallagher, E. L., Elgar, S., & Guza, R. T. (1998). Observations of sand bar evolution on a natural beach. *Journal of Geophysical Research*, *103*(C2), 3203–3215. https://doi.org/10.1029/97JC02765

Grant, W. D., & Madsen, O. S. (1979). Combined wave and current interaction with a rough bottom. *Journal of Geophysical Research*, *84*(C4), 1797–1808. https://doi.org/10.1029/jc084ic04p01797

Guerrero, Q., Williams, M., Guillén, J., Lichtman, I., Thorne, P., & Amoudry, L. (2021). Small-scale bedforms and associated sediment transport in a macro-tidal lower shoreface. *Continental Shelf Research*, *225*, 104483. https://doi.org/10.1016/j.csr.2021.104483

Hanes, D. M., Alymov, V., Chang, Y. S., & Jette, C. (2001). Wave-formed sand ripples at Duck, North Carolina. *Journal of Geophysical Research*, *106*(C10), 22575–22592. https://doi.org/10.1029/2000JC000337

Haubrich, R. A. (1965). Earth noise, 5 to 500 millicycles per second: 1. Spectral stationarity, normality, and nonlinearity. *Journal of Geophysical Research*, *70*(6), 1415–1427. https://doi.org/10.1029/JZ070i006p01415

Hegge, B. A., Eliot, M. J., & Hsu, J. (1996). Sheltered sandy beaches of southwestern Australia. *Journal of Coastal Research*, *12*, 748–760.

Hoefel, F., & Elgar, S. (2003). Wave-induced sediment transport and sandbar migration. *Science*, *299*(5614), 1885–1887. https://doi.org/10.1126/science.1081448

Hoekstra, P., Bell, P., Van Santen, P., Roode, N., Levoy, F., & Whitehouse, R. (2004). Bedform migration and bedload transport on an intertidal shoal. *Continental Shelf Research*, *24*(11), 1249–1269. https://doi.org/10.1016/j.csr.2004.03.006

Hurther, D., & Thorne, P. D. (2011). Suspension and near-bed load sediment transport processes above a migrating, sand-rippled bed under shoaling waves. *Journal of Geophysical Research*, *116*(C7), 2010JC006774. https://doi.org/10.1029/2010JC006774

John, J. A., & Draper, N. R. (1980). An alternative family of transformations. *Applied Statistics*, *29*(2), 190. https://doi.org/10.2307/2986305

Kalra, T. S., Suttles, S. E., Sherwood, C. R., Warner, J. C., Aretxabaleta, A. L., & Leavitt, G. R. (2022). Shoaling wave shape estimates from field observations and derived bedload sediment rates. *Journal of Marine Science and Engineering*, *10*(2), 223. https://doi.org/10.3390/jmse10020223

Kranenburg, W. M., Ribberink, J. S., Schretlen, J. J. L. M., & Uittenbogaard, R. E. (2013). Sand transport beneath waves: The role of progressive wave streaming and other free surface effects. *Journal of Geophysical Research: Earth Surface*, *118*(1), 122–139. https://doi.org/10.1029/2012JF002427

Kranenburg, W. M., Ribberink, J. S., Uittenbogaard, R. E., & Hulscher, S. J. M. H. (2012). Net currents in the wave bottom boundary layer: On waveshape streaming and progressive wave streaming. *Journal of Geophysical Research*, *117*(F3), 2011JF002070. https://doi.org/10.1029/2011JF002070

Longuet-Higgins, M. S. (1953). Mass transport in water waves. *Philosophical Transactions of the Royal Society of London - Series A: Mathematical and Physical Sciences*, *245*(903), 535–581. https://doi.org/10.1098/rsta.1953.0006

Lygre, A., & Krogstadt, H. (1986). Maximum entropy estimation of the directional distribution in ocean wave spectra. *Journal of Physical Oceanography*, *16*(12), 2052–2060. https://doi.org/10.1175/1520-0485(1986)016<2052:meeotd>2.0.co;2

Makaske, B., & Augustinus, P. G. E. F. (1998). Morphologic changes of a micro-tidal, low wave energy beach face during a spring-neap tide cycle, Rhône-Delta, France. *Journal of Coastal Research*, *14*, 632–645.

Marin, F. (2004). Eddy viscosity and Eulerian drift over rippled beds in waves. *Coastal Engineering*, *50*(3), 139–159. https://doi.org/10.1016/j.coastaleng.2003.10.001

Masselink, G., Austin, M. J., O'Hare, T. J., & Russell, P. E. (2007). Geometry and dynamics of wave ripples in the nearshore zone of a coarse sandy beach. *Journal of Geophysical Research*, *112*(C10), 2006JC003839. https://doi.org/10.1029/2006JC003839

Meyer-Peter, E., & Mueller, R. (1948). Formulas for bed-load transport. In *Proceedings of the IAHR* (pp. 39–64).

Mieras, R. S., Puleo, J. A., Anderson, D., Hsu, T. J., Cox, D. T., & Calantoni, J. (2019). Relative contributions of bed load and suspended load to sediment transport under skewed-asymmetric waves on a sandbar crest. *Journal of Geophysical Research: Oceans*, *124*(2), 1294–1321. https://doi.org/10.1029/2018JC014564

Mignot, E., Hurther, D., Chassagneux, F. X., & Barnoud, J. M. (2011). A field study of the ripple vortex shedding process in the shoaling zone of a macro-tidal sandy beach. *Journal of Coastal Research*, *SI56*, 1776–1780.

Miles, J., Thorpe, A., Russell, P., & Masselink, G. (2014). Observations of bedforms on a dissipative macrotidal beach. *Ocean Dynamics*, *64*(2), 225–239. https://doi.org/10.1007/s10236-013-0677-2

Miller, M. C., & Komar, P. D. (1980). A field investigation of the relationship between oscillation ripple spacing and the near-bottom water orbital motions. *Journal of Sedimentary Research*, *50*(1), 183–191. https://doi.org/10.2110/jsr.50.183

Nelson, T. R., Voulgaris, G., & Traykovski, P. (2013). Predicting wave-induced ripple equilibrium geometry. *Journal of Geophysical Research: Oceans*, *118*(6), 3202–3220. https://doi.org/10.1002/jgrc.20241

Ngusaru, A. S., & Hay, A. E. (2004). Cross-shore migration of lunate megaripples during Duck94. *Journal of Geophysical Research*, *109*(C2), 2002JC001532. https://doi.org/10.1029/2002JC001532

Nielsen, P. (1981). Dynamics and geometry of wave-generated ripples. *Journal of Geophysical Research*, *86*(C7), 6467–6472. https://doi.org/10.1029/JC086iC07p06467

Nnadi, F. N., & Wilson, K. C. (1992). Motion of contact-load particles at high shear stress. *Journal of Hydraulic Engineering*, *118*(12), 1670–1684. https://doi.org/10.1061/(ASCE)0733-9429(1992)118:12(1670)

Nordstrom, K. F., & Jackson, N. L. (2012). Physical processes and landforms on beaches in short fetch environments in estuaries, small lakes and reservoirs: A review. *Earth-Science Reviews*, *111*(1–2), 232–247. https://doi.org/10.1016/j.earscirev.2011.12.004

Núñez-González, F., & Martín-Vide, J. P. (2011). Analysis of antidune migration direction. *Journal of Geophysical Research*, *116*(F2), 2010JF001761. https://doi.org/10.1029/2010JF001761

Osborne, P. D., & Greenwood, B. (1992). Frequency dependent cross-shore suspended sediment transport. 1. A non-barred shoreface. *Marine Geology*, *106*(1–2), 1–24. https://doi.org/10.1016/0025-3227(92)90052-J

Perk, L., van Rijn, L., Koudstaal, K., & Fordeyn, J. (2019). A rational method for the Design of Sand Dike/Dune Systems at Sheltered Sites; Wadden Sea Coast of Texel, the Netherlands. *Journal of Marine Science and Engineering*, *7*(9), 324. https://doi.org/10.3390/jmse7090324

Plant, N. G., Holland, K., & Puleo, J. A. (2002). Analysis of the scale of errors in nearshore bathymetric data. *Marine Geology*, *191*(1–2), 71–86. https://doi.org/10.1016/S0025-3227(02)00497-8

Puleo, J. A., Lanckriet, T., & Wang, P. (2012). Near bed cross-shore velocity profiles, bed shear stress and friction on the foreshore of a microtidal beach. *Coastal Engineering*, *68*, 6–16. https://doi.org/10.1016/j.coastaleng.2012.04.007

Ribberink, J. S. (1998). Bed-load transport for steady flows and unsteady oscillatory flows. *Coastal Engineering*, *34*(1–2), 59–82. https://doi.org/10.1016/S0378-3839(98)00013-1

Ribberink, J. S., Van Der Werf, J. J., O'Donoghue, T., & Hassan, W. N. (2008). Sand motion induced by oscillatory flows: Sheet flow and vortex ripples. *Journal of Turbulence*, *9*, N20. https://doi.org/10.1080/14685240802220009

Ruessink, B., Houwman, K., & Hoekstra, P. (1998). The systematic contribution of transporting mechanisms to the cross-shore sediment transport in water depths of 3 to 9 m. *Marine Geology*, *152*(4), 295–324. https://doi.org/10.1016/S0025-3227(98)00133-9

Schretlen, J. (2012). *Sand transport under full-scale progressive surface waves* (PhD thesis). University of Twente. https://doi.org/10.3990/1.9789462030619

Sleath, J. F. A. (1999). Conditions for plug formation in oscillatory flow. *Cpntinental Shelf Research*, *19*(13), 1643–1664doi. https://doi.org/10.1016/S0278-4343(98)00096-X

Soulsby, R. (1997). *Dynamics of marine sands*. Thomas Telford Ltd. https://doi.org/10.1680/doms.25844

Swart, D. (1974). Offshore sediment transport and equilibrium beach profiles. Technical report 131. Delft hydraulics. Delft.

Talmon, A., Struiksma, N., & Van Mierlo, M. (1995). Laboratory measurements of the direction of sediment transport on transverse alluvial-bed slopes. *Journal of Hydraulic Research*, *33*(4), 495–517. https://doi.org/10.1080/00221689509498657

Talmon, A. M., & Wiesemann, J. (2006). Influence of grain size on the direction of Bed- load transport on transverse sloping beds. In *Proceedings 3rd international conference on scour and erosion, Gouda, the Netherlands* (pp. 632–639).

Thorne, P. D., Davies, A. G., & Williams, J. J. (2003). Measurements of near-bed intra-wave sediment entrainment above vortex ripples. *Geophysical Research Letters*, *30*(20), 2003GL018427. https://doi.org/10.1029/2003GL018427

Travers, A. (2007). Low-energy beach morphology with respect to physical setting: A case study from cockburn sound, Southwestern Australia. *Journal of Coastal Research*, *232*, 429–444. https://doi.org/10.2112/04-0275.1

Traykovski, P. (2007). Observations of wave orbital scale ripples and a nonequilibrium time-dependent model. *Journal of Geophysical Research*, *112*(C6), 2006JC003811. https://doi.org/10.1029/2006JC003811

Traykovski, P., Hay, A. E., Irish, J. D., & Lynch, J. F. (1999). Geometry, migration, and evolution of wave orbital ripples at LEO-15. *Journal of Geophysical Research*, *104*(C1), 1505–1524. https://doi.org/10.1029/1998JC900026

Trowbridge, J. H., & Lentz, S. J. (2018). The bottom boundary layer. *Annual Review of Marine Science*, *10*(1), 397–420. https://doi.org/10.1146/annurev-marine-121916-063351

Van Der Lugt, M., de Schipper, M., Reniers, A., Fritsch, N., & Wengrove, M. (2026). Data underlying the publication: Observations of intermittent cross-shore bed load transport on a low-energy beach [Dataset]. *TU Delft - 4TU.ResearchData*. https://doi.org/10.4121/ad1ad426-3c19-43a1-a4b6-c726426bc53a

Van Der Lugt, M., De Schipper, M., Reniers, A., & Ruessink, B. (2024a). Parametrizing nonlinearity in orbital velocity at fetch-limited, low-energy beaches. *Coastal Engineering*, *194*, 104602. https://doi.org/10.1016/j.coastaleng.2024.104602

Van Der Lugt, M. A., Bosma, J. W., De Schipper, M. A., Price, T. D., Van Maarseveen, M. C. G., Van Der Gaag, P., et al. (2024). Measurements of morphodynamics of a sheltered beach along the Dutch Wadden Sea. *Earth System Science Data*, *16*(2), 903–918. https://doi.org/10.5194/essd-16-903-2024

Van Der Werf, J. J., Doucette, J. S., O'Donoghue, T., & Ribberink, J. S. (2007). Detailed measurements of velocities and suspended sand concentrations over full-scale ripples in regular oscillatory flow. *Journal of Geophysical Research*, *112*(F2), 2006JF000614. https://doi.org/10.1029/2006JF000614

Van Der Werf, J. J., Ribberink, J. S., O'Donoghue, T., & Doucette, J. S. (2006). Modelling and measurement of sand transport processes over full-scale ripples in oscillatory flow. *Coastal Engineering*, *53*(8), 657–673. https://doi.org/10.1016/j.coastaleng.2006.02.002

Van Der Zanden, J., Van Der A, D., Hurther, D., Cáceres, I., O'Donoghue, T., & Ribberink, J. (2017). Suspended sediment transport around a large-scale laboratory breaker bar. *Coastal Engineering*, *125*, 51–69. https://doi.org/10.1016/j.coastaleng.2017.03.007

Van Rijn, L. C. (2007). Unified view of sediment transport by currents and waves. I: Initiation of motion, bed roughness, and bed-load transport. *Journal of Hydraulic Engineering*, *133*(6), 649–667. https://doi.org/10.1061/(ASCE)0733-9429(2007)133:6(649)

Vila-Concejo, A., Fellowes, T. E., Gallop, S., Alejo, I., Angnuureng, D. B., Benavente, J., et al. (2024). Morphodynamics and management challenges for beaches in modified estuaries and bays. *Cambridge Prisms: Coastal Futures*, *2*, e11. https://doi.org/10.1017/cft.2024.7

Vila-Concejo, A., Gallop, S. L., & Largier, J. L. (2020). Sandy beaches in estuaries and bays. In *Sandy beach morphodynamics* (pp. 343–362). Elsevier. https://doi.org/10.1016/B978-0-08-102927-5.00015-1

Wang, D., & Yuan, J. (2020). An experimental study of net sediment transport rate due to acceleration-skewed oscillatory flows over rippled seabeds. *Coastal Engineering*, *155*, 103583. https://doi.org/10.1016/j.coastaleng.2019.103583

Wengrove, M. E., Foster, D. L., de Schipper, M. A., & Lippmann, T. C. (2017). Wave and current ripple formation and migration during storms. In *Proceedings of Coastal Dynamics* (Vol. 129, pp. 955–965).

Wengrove, M. E., Foster, D. L., Lippmann, T. C., de Schipper, M. A., & Calantoni, J. (2018). Observations of time-dependent bedform transformation in combined wave-current flows. *Journal of Geophysical Research: Oceans*, *123*(10), 7581–7598. https://doi.org/10.1029/2018JC014357

Yuan, J. (2023). Observations of net sediment transport rate and boundary layer of wave–current flows over vortex ripples. *Coastal Engineering*, *181*, 104288. https://doi.org/10.1016/j.coastaleng.2023.104288